Energetic Particles and Acceleration Regions over Jupiter's Polar Cap and Main Aurora; a Broad Overview

B. H. Mauk[1], G. Clark[1], G. R. Gladstone[2], S. Kotsiaros[3,4], A. Adriani[5], F. Allegrini[2,6], F. Bagenal[7], S. J. Bolton[2], B. Bonfond[8], J. E. P. Connerney[3,9], R. W. Ebert[2], D. K. Haggerty[1], P. Kollmann[1], W. S. Kurth[10], S. M. Levin[11], C. P. Paranicas[1], A. M. Rymer[1]

[1]The Johns Hopkins University Applied Physics Laboratory, Laurel, Maryland, USA (Barry.Mauk@jhuapl.edu)

[2]Southwest Research Institute, San Antonio, Texas, USA

[3]NASA Goddard Space Flight Center, Greenbelt, Maryland, USA

[4]University of Maryland College Park, College Park, MD, USA

[5]Instituto Nazionale di Astrofisica-Instituo di Astofisica e Planetologia Spaziali, Roma, Italy

[6]Physics and Astronomy Department, University of Texas at San Antonio, Texas, USA

[7]University of Colorado, Laboratory for Space and Atmospheric Sciences, Boulder, Colorado, USA

[8]Université de Liège, Technologies and Astrophys. Res. Institute, LPAP,, Liège, Belgium

[9]Space Research Corporation, Annapolis, Maryland, USA

[10]University of Iowa, Iowa City, Iowa, USA

[11]Jet Propulsion Laboratory, Pasadena, California, USA

Corresponding author: Barry H. Mauk (Barry.Mauk@jhuapl.edu)

Key Points:

- Jupiter's polar caps have upward electron beams essentially everywhere (100's of keV), and often downward megavolt electric potentials.
- Energetic particles reveal 3 main auroral acceleration zones: diffuse aurora (DifA), Zone-I (Downward), and Zone-II (Bi-directional).
- ZI(D) and ZII(B) sometimes (but not always) contain, respectively, downward electron inverted-V's and downward proton inverted-Vs.

Abstract

Previous Juno mission event studies revealed powerful electron and ion acceleration, to 100's of keV and higher, at low altitudes over Jupiter's main aurora (MA) and polar cap (PC; poleward of the main aurora). Here we examine 30 – 1200 keV JEDI-instrument particle data from the first 16 Juno orbits to determine how common, persistent, repeatable, and ordered these processes are. For the PC regions we find: 1) Upward electron angle beams, sometimes extending to MeV energies, are persistently present in essentially all portions of the polar cap, but are generated by two distinct and spatially separable processes. 2) Particle evidence for megavolt downward electrostatic potentials are observable for 80% of the polar cap crossings and over substantial fractions of the PC area. For the main aurora, with the orbit favoring the dusk side, we find: 1) Three distinct zones are observed that are generally arranged from lower to higher latitudes but sometimes mixed. They are designated here as the diffuse aurora (DifA), Zone-I (ZI(D)) showing primarily downward electron acceleration, and Zone-II (ZII(B)) showing bi-directional acceleration with the upward intensities often greater than downward intensities. 2) ZI(D) and ZII(B) sometimes (but not always) contain, respectively, downward electron inverted-V's and downward proton inverted-V's, (potentials up to 400 kV), but otherwise have broadband distributions. 3) Surprisingly, both ZI(D) and ZII(B) can generate equally powerful auroral emissions. It is suggested, but demonstrated for intense portions of only one auroral crossing, that ZI(D) and ZII(B) are associated, respectively, with upward and downward electric currents.

Plain Language Summary

The science objectives of the Juno mission, with its spacecraft now orbiting Jupiter in a polar orbit, include understanding the space environments of Jupiter's polar regions and generation of Jupiter's uniquely powerful aurora. In Jupiter's polar cap regions (poleward of the main auroral oval encircling the northern and southern poles) we find here that: 1) beams of electrons aligned with the upward magnetic field direction are ever-present with energies extended to the 100's to 1000's of kilo electron volts; and 2) downward magnetic field-aligned electrostatic potentials reaching greater than a million volts occur over broad regions for 80% of the polar cap crossings. For the main auroral oval, we find three distinct zones; designated here as diffuse aurora (DifA), Zone-I (ZI(D)) showing downward electron acceleration to 100's of kilo-electron-volts, and Zone-II (ZII(B)) showing bi-directional acceleration with the upward intensities often greater than downward intensities. ZI(D) sometimes shows upward electrostatic potentials reaching 100's of kilovolts, and is associated with upward magnetic field-aligned electric currents. ZII(B) sometimes shows downward electrostatic potentials reaching 100's of kilovolts, and is associated with downward electric currents. Unexpectedly from Earth studies, ZI(D) and ZII(B) are just as likely to generate the most intense auroral emissions.

1 Introduction and Background

Previous studies coming as a result of the Juno polar-orbiting mission to Jupiter (Bolton et al. 2017a) have revealed surprising energetic particle features within both the main auroral (MA) regions and the polar cap (PC) regions (defined here as simply those regions poleward of the main aurora). Within the polar cap, high energy electron beams, with power-law-like distributions up to MeV energies, were observed streaming narrowly along upward magnetic field lines over broad spatial regions (Mauk et al., 2017a; Paranicas et al., 2018; Bonfond et al., 2018). These beams may be the source of some of the upward beams observed by the Ulysses spacecraft for high altitude, mid-latitudes reported by Lanzerotti et al. (1993). The Juno beams

were often accompanied by strong whistler waves (Tetrick et al., 2017) that were shown to have a substantial scattering impact on the beams (Elliott et al., 2018). Haggerty et al. (2017) observed broad regions of precipitating heavy ions (O and S) narrowly confined to field-aligned pitch angles. Clark et al. (2017a) used ion measurements to reveal the presence of downward megavolt potentials over large spatial regions. Smaller potentials were revealed with up-going electron "inverted Vs"; localized regions of magnetic field-aligned electrostatically accelerated electrons. Clark et al. (2017b) presented a novel energetic ion conic event over the polar cap. At lower energies, the polar cap revealed a number of distinctly different regions, including regions of multiplicities of upward electron inverted-V's, seemingly much more structured than apparent in the higher energies (Ebert et al., 2017). At these lower energies, there are regions with field-aligned beams of upward and downward electrons that are broad in energy. Observations in the ultraviolet reveal several sub-regions in the polar cap, including a distinct central area showing strong methane absorption signatures, suggestive of precipitating high energy particles (Bonfond et al. 2017).

Over the main auroral oval the Juno teams were surprised by two distinct aspects of the measurements. Early measurements showed that strong auroral emissions are generated by broadband electron distributions rather than the "inverted-V" distributions that were anticipated as a result of expected magnetic field-aligned electric potentials (Allegrini et al., 2017; Connerney et al., 2017a; Mauk et al., 2017a). Additionally, the magnetic field-aligned electric currents were much weaker than expected on the basis of comparisons with Earth (Connerney et al., 2017a). More recently, inverted-V distributions were observed over the MA, but none-the-less the most intense auroras were still generated by broadband processes (Mauk et al., 2017b). Other peculiarities have also been observed whereby intense downward electron energy fluxes are accompanied by powerful downward electric potentials (up to 300 kV) above the spacecraft (Mauk et al., 2018). And still more recently the magnetic field-aligned currents have been quantitatively measured with several unexpected elements, including high degrees of structuring in the azimuthal directions and strong asymmetries between the northern regions (weak currents) and the southern regions (strong currents) (Kotsiaros et al., 2019).

What has been missing is an understanding of how all of these features fit into a larger picture. In performing event studies one tends to focus on intense and unusual features without establishing the commonality, repeatability, and importance of the various features that are observed. Here we examine those aspects of the features by examining more completely the first 16 orbits (the first half of the prime Juno mission) of the energetic particle measurements made over the northern and southern polar regions. We find that the energetic particles within the polar regions (PC+MA) are more ordered and repeatable than was realized during the earlier investigations.

In the following sections we discuss the Juno mission and measurements in general (Section 2), we focus on energetic particle measurements made within the Polar Cap (PC) regions, including a summary of the PC findings (Section 3), followed by a focus on energetic particle measurements made over the Main Aurora (MA), including a summary of MA findings (Section 4), followed finally with discussion of the implications of our findings (Section 5).

2 Measurements and Orbital Configuration

2.1 The Juno mission

The Juno mission was launched in 2011, and was inserted into Jupiter orbit in July of 2016 with the following characteristics: 1.05 x 112 RJ polar (~90° inclination), ~53.5 day period elliptical orbit with the line-of-apsides close to the dawn equatorial meridian. Following insertion, the line-of-apsides has been slowly precessing southward (~ 1° per orbit) and towards the nightside (~4° per orbit). Juno targets multiple disciplines including Jupiter's interior, atmosphere, polar space environment and its powerful aurora (Bolton et al.; 2017a; Bagenal et al., 2017). Initial findings from the Juno mission for all disciplines were presented by Bolton et al. (2017b) and Connerney et al. (2017a).

Figure 1b shows the inner portion of Juno's first orbit (Perijove 1, or PJ1) as diagrammed in polar magnetic coordinates using the JRM09 internal magnetic field (Connerney et al., 2018) and an explicit magnetodisc model (Connerney et al., 1981) for the external magnetic field. When the elliptical Juno orbit is replotted in a coordinate system with the z-axis aligned with the magnetic dipole, there is a wiggle appearance to the trajectory due to the rocking in magnetic latitude as Jupiter's rotation sweeps the tilted dipole past the spacecraft. The spacecraft passes over Jupiter's main auroral regions and polar cap at very low altitudes during transit. When the position of the spacecraft is mapped down to the atmosphere along magnetic field lines, the result is like that shown in Figure 2a. Here is an image of the northern aurora obtained by the Ultraviolet Spectrograph (UVS; Gladstone et al., 2017a) with the magnetic projection of the Juno orbital trajectory shown with the thin cyan line (it appears dotted where the spacecraft moves most rapidly). That line crosses the main aurora in several places and spends substantial time within the often less UV-bright polar cap regions. Of particular interest is the very last main auroral crossing as the trajectory passes out of the picture (see white arrow on the right for this particular case). That last crossing of the main aurora (or first crossing of the main aurora in the southern hemisphere) occurs at the lowest altitudes, generally below 1 RJ altitude or 2 RJ from Jupiter's center. Since that low altitude crossing tends to occur on the dusk side, our main auroral results here favor dusk-side measurements.

2.2 Juno measurements

We focus in this study on measurements from the Jupiter Energetic-particle Detector Instrument (JEDI) which measures energy, angular, and compositional distributions of electrons (~ 25 to ~1200 keV) and ions (protons: ~10 keV to > 1.5 MeV; oxygen and sulfur from ~150 keV to > 10 MeV)). JEDI uses solid state detectors (SSDs), thin foils, and Microchannel Plate detectors (MCPs) to measure electron SSD singles rates (SSDs shielded by 2μ Al), time-of-flight by energy (TOFxE) for higher energy ions, and time-of-flight by MCP pulse height (TOFxPH) for lower energy ions (Mauk et al., 2017c). JEDI is a complement to the lower energy Jupiter Auroral Distributions Experiment (JADE) instrument, which measures distributions of electron from 100 eV to 100 keV, and of ions with composition up to 46 keV/q, where q is electric charge (McComas et al., 2017). Some initial results from the JADE instrument over auroral regions and the polar caps are provided by Allegrini et al. (2017), Szalay et al. (2017), and Ebert et al. (2017; 2019). Of special importance to our investigation here is the magnetometer (MAG) measurements (Connerney et al. 2017b) which allow particle measurements to be ordered by pitch angle (angle between the particle velocity vector and the magnetic field vector).

Additionally, the magnetometer can be used to infer magnetic field-aligned currents, recently described by Kotsiaros et al., (2019). Finally, the magnetometer instrument can be used to study aspects of Alfvénic turbulence that might play a role in auroral particle acceleration (Gershman et al., 2019). The UVS instrument is critical to providing the auroral context for the particle measurements. Initial results from the UVS instrument team are provided by Gladstone et al. (2017b) and Bonfond et al., (2017). Infra-red images of the aurora are obtained by the Jovian Infrared Auroral Mapper (JIRAM) instrument (Adriani et al., 2017; see initial images in Mura et al., 2017). Ultimately one also wishes to compare downward particle energy fluxes with auroral intensities. Initial studies of such comparisons have been achieved by Ebert et al. (2019), Gérard et al. (2019), and Allegrini et al. (2019). It will not be a focus of the present study, but ultimately the understanding of the acceleration processes associated with the features identified here will depend on the characterization of the plasma waves that accompany the features, as diagnosed with the Waves instrument (Kurth et al., 2017). Early results on the relationships between auroral and polar cap particle features and wave phenomena can be found in Tetrick et al. (2017) and Elliot et al., (2018a and 2018b) for the polar cap, and in Kurth et al. (2018) for the main aurora. These results highlight an important role for whistler waves, whereas at Earth the greater focus has been on Alfvén waves.

2.3 JEDI challenges

A critical aspect of the Juno JEDI measurements for the study presented here is the challenge of obtaining complete pitch angle distributions in a short enough time to characterize spatially narrow features. Close to Jupiter Juno travels over 50 km/s and spins at a rate of 2 RPM (30 second spin periods). Hence, during one complete spin the spacecraft travels on the order of 1500 km, much broader than many main auroral features. JEDI does obtain pitch angle distributions in much shorter time intervals through the use of multiple telescopes, but some loss of spatial resolution is inescapable nevertheless. JEDI consists of 3 independent instruments each of which has 6 telescopes arranged in a ~160° fan. The configuration of these three instruments (JEDI-90 or J90, J180, and J270) is shown in Figure 1a. J90 and J270 are oriented to approximate a 360° field of view within a plane roughly perpendicular to the spacecraft spin vector. When the magnetic field line is contained within that plane, the 360° view provides a workable pitch angle distribution at every instant of time. However, the 160° fans do not reside exactly perpendicular to the spin axis; they have been tilted and twisted by up to 10° to avoid viewing the huge solar panels. The most complete pitch angle coverage is obtained with 30 second averages, but often 30 seconds is too long to resolve important main auroral features. Investigation of auroral features requires that one optimize the choice between time resolution and pitch angle sampling. We have found that showing both 30 second and 5 second averages seems to do the best job for present purposes. Higher time resolution is required for other studies, like those event studies that have been previously cited, to investigate the true energy fluxes and auroral structuring.

The nominal jovian magnetic field is approximately normal to the spacecraft spin vector (which most often points towards Earth) only while Juno's orbit is near the dawn-dusk meridian. That optimal situation degrades as the orbit local time evolves towards the night side. For studies of the polar cap, where 30 second averages suffice for the broad structures that are addressed here, a reasonably good job of capturing the pitch angle distributions is done for orbits 1-16 (no science data was obtained close to Jupiter for orbit 2). The pitch angle sampling

degraded substantially after that time. For the main aurora, where higher time resolution is required, the pitch angle sample degrades very substantially after about orbit 10, and so for those studies we confine ourselves to the first 10 orbits. Because of the orientation of the third of the 3 JEDI instruments (J180; see Figure 1a), fairly complete pitch angle sampling for electrons is obtained with 30 second resolution for all other orbits. However, J180 does not have an ion measurement capability. During an extended mission, good pitch angle sampling will return as the orbit evolves towards the dusk meridian. That region is centered on about orbit 45, allowing for fair to very good pitch angle coverage for orbits 35-55.

The full-width at half maximum angle (FWHM) resolution of JEDI is roughly 17°x9°, with the 17° dimension oriented along the 160° fan. In high resolution mode, JEDI accumulates for 0.25 seconds at a cadence of 0.5 seconds (ions and electron measurements are sub-commutated). Hence, during an accumulation the field-of-view is smeared by 3° (which, for J90 and J270 does not substantially alter the FWHM). An important issue is whether or not the resolution element (or telescope) is fully contained within the loss cone at low altitudes. In the present paper we use a rough estimate of the loss cone based on the expression provided by Mauk et al. (2017a) derived from conservation of the first adiabatic invariant and assuming that the magnetic field varies roughly as R^{-3}. We find: LC-angle ~ $Sin^{-1}(1/R^3)^{1/2}$, where R is radial position (from the center of Jupiter) in units of RJ. This expression does a fairly good job of representing the loss cones that are most sharply defined in the ion data (Mauk et al., 2017a). For R = 2, the loss cone is very roughly 20°-21°, which means that the full cone opening is 40°-42°, easily able to contain the JEDI telescope field-of-view. The maximum altitude (using this simple expression) which allows the JEDI field of view (with luck) to be contained within the loss cone is 3.5 RJ, although a more safe value would be 2.7 RJ, corresponding to where the loss cone contains 1.5 JEDI resolution elements. When showing pitch angle distributions, we often use a resolution element of 4.5° (half of the 9° FWHM in the sideways dimension) so that when the elements closest to 0° or 180° are filled, we know that the field line was contained within the JEDI field-of-view for a portion of that accumulation period.

Other challenges for the JEDI measurements are worthy of note here. As described in some detail in the Mauk et al. (2018) Supporting Information (Section S1), MeV-class electrons (starting weakly at 0.4 MeV) can fully penetrate the solid state detectors (SSDs) and leave behind only a fraction of their full energies, known colloquially as the minimum ionizing energy. For JEDI with 0.5 mm SSDs, the peak of that energy is about 160 keV (see the horizontal enhancement labeled “MeV e- pen.” centered at about 160 keV in Figure 3c). The presence of that peak is clear evidence that the electron distributions are very energetic, extending into the multiple MeV range, as also evidenced by analysis of penetrating electrons across several of the Juno instruments (Becker et al., 2017). Despite the fact that these electrons penetrate the SSD, these are still foreground electrons that have come through the collimator of the sensor; JEDI is shielded from side penetrators for energies of 10-15 MeV depending on directionality. The minimum ionizing peak can have the appearance of being the result of electrostatic auroral acceleration (e. g. from so-called Inverted-V configurations). However, we have learned that when true electrostatic acceleration is present, there are almost never enough MeV class electrons to generate a minimum ionizing feature (Mauk et al., 2018 Supporting information S3). We have developed robust procedures for correcting the spectra and for cleanly discriminating between penetrators and auroral acceleration, as described in the Mauk et al., 2018 Supporting information Sections S1 and S3. Those procedures are applied to individual spectra; we do not

yet have a reliable blind automated procedure to apply them to the color spectrograms. But on the spectrograms, this feature is very useful in realizing at a glance just how energetic the distributions are.

Electrons that stimulate each of the 6 telescopes within each instrument cross paths on their ways from the JEDI collimator to each of the 6 SSDs. This condition was necessary given the need for multiplicities of telescopes while minimizing instrument resources such as mass. Therefore, electrons can scatter on foils, grids, and other internal surfaces and find their ways to unintended SSDs. This process limits the contrast between signal and noise. Figure 2b shows a sample of the electron beams that we will be discussing, but also shows the result of scattering in terms of a noise floor (See also Mauk et al. 2018 Supporting Information Section S7).

3 Polar Cap Regions

Two specific phenomena are of greatest interest here for the characterization of the polar cap regions. First are the upward, narrowly collimated, broadband electron beams streaming out of at least portions of the polar cap as first studied for one orbit by Mauk et al. (2017a). Second are the large-scale, downward, magnetic field-aligned electrostatic potentials often exceeding megavolt levels (Clark et al., 2017a). Our task is to use the first 16 orbits of Juno to determine how common and persistent such features are. Here we are not addressing a range of other phenomena that have been reported for the polar cap. For example, while the polar cap regions tend to be relatively dark (in the UV; Figure 2a), there are dynamic auroral emissions that can occur over broad regions, but also including an intense, spatially confined "flare" region thought to map to Jupiter's polar cusp (Grodent et al., 2003; Grodent 2015).

3.1 Polar cap electron beam characteristics

The upward electron beams are illustrated in Figure 2. Figure 2a shows the projected trajectory of Juno, and Figure 2d shows a measure of the response of the JEDI electron sensors to the various regions visited. Figure 2d is the average intensity of the electrons over a broad range of energies (30-1000 keV) plotted as a function of "azimuth" angle. Azimuth is defined in Figure 1a, and is used as a proxy for pitch angle. We sometime use azimuth because the electron beams are so narrow that they hug the axis of the pitch angle plots, making it difficult to discern the nature of the beams.

We see in Figure 2d, from left to right, the passage of Juno from the horns of the radiation belt, into relatively intense bi-directional electron beams associated with the main aurora as it appears to JEDI from high altitude (~7 RJ), then into much lower intensity bi-directional electron populations, through about 0900. Juno then enters what we call the polar cap where the prominent feature within the JEDI data are very narrow upward-going electron beams. Figure 2b shows just how narrow those beams are in pitch angle; they are narrow enough so that JEDI does not properly resolve them. Hence, the intensity values are likely under-estimated (see the Mauk et al., 2018 Supporting Information Section S6). Figure 2c shows that the intensity spectra are power-law in nature extending in energy to above 1 MeV; these spectra are the result of an inversion process that removes the minimum ionizing feature that peaks at 160 keV (see Supporting Information in Mauk et al., 2018, Section S1). As we continue on to the right in Figure 2d, we encounter lower intensity downward electron beams that accompany the upward beams starting at about 1130. This downward component may possibly represent: i) the

magnetically reflected return of the upward beams, ii) the consequence of beams generated on the opposite hemisphere, or iii) evidence of associated downward acceleration as we dip into a broad acceleration region at lower altitudes. It was hypothesized by Mauk et al. (2017a) that the field lines near the center of the polar cap are so long that the electron beams are scattered to non-existence by the time the full field-line was traversed. Elliot et al. (2018) provided evidence that the scattering takes place as a result of whistler waved observed concurrently and that the scattering can be substantial over distances of just several jovian radii. On shorter field lines, it might be possible that beams from the opposite hemisphere, or from magnetic reflection, may be retained.

Ebert et al. (2019) favors the hypothesis that the electron beam acceleration is bi-directional (at least in some places) and that the downward component will continue to become more prominent as one dips closer and closer to the planet. In favor of that hypothesis is their finding that structured polar cap auroral emissions that they studied for one particular perijove (PJ5) could be explained if the downward component of the beams at lower altitudes carried electron energy fluxes that were similar to the energy fluxes carried by the upward beams at the Juno location.

3.2 Polar cap electron beam overview

To accomplish the task of determining the prevalence and persistence of the beams, we have generated overview plots for the first 16 orbits (absent PJ2). Three of these plots are shown in Figures 3-5, showing the northern hemisphere on the left and the southern hemisphere on the right. Panels (b), (c), and (d) show 30 second averages of energetic electron data: azimuth distributions, energy distributions for upgoing electrons (within 15° of the magnetic field line), and estimates of both up-going and down-going electron energy fluxes. Most telling is Panel (d) which provides some quantitative measure of the electron beams. Figures 4 and 5 show similar plots for PJ3 and PJ8. With these survey plots and the other 12 survey plots not shown, we find that the upward electron beams are almost always present in all portions of the polar caps. However, the main aurora sometimes represents an intensification of the upward beams with a more substantial downward component. Thus, the beams do not necessarily provide a clear demarcation between the polar cap and portions of the main aurora.

The upward electron beams evidence broad spatial scale variations in their intensities. In Figure 3d we see the upward energy flux increasing from left to the middle of the figure, and decreasing to the far right. We believe that this is a consequence of spacecraft altitude. This feature is mostly repeated in the other survey plots, particularly in the south where Juno traverses the greatest range of altitudes (because of the precession of the orbit over time). Elliott et al. (2018a) has shown that concurrent whistler waves scatter the electrons in pitch angle as the particles move upward along the field lines. However, because JEDI does not resolve the beams and because the pitch angle sampling for unresolved beams is complicated, we are uncertain as to whether simple scattering would lower the average “measured” intensity. It is possible that when Juno is at lower altitudes it is dipping deeper into an acceleration region that has some extent in altitude. Such a conclusion is favored by the results of Ebert et al (2019) who found that altitude affects the relative magnitude of upward and downward energy fluxes of < 100 keV electrons (see also the appearance of bi-directional beams at the lower altitudes in Figures 2d and 3b).

While the polar cap electron beams seem to be ever-present, they do vary in a fashion beyond the gradual, altitude-dependent variation discussed in the previous paragraph. The beams are temporally variable, even spiky, over much shorter time periods, and this spikiness is somewhat correlated with whistler wave variations (Tetrick et al., 2017). Additionally, Paranicas et al. (2018) have identified periods of particularly energetic beams within the so-called swirl regions of the polar cap (see review of polar cap emissions by Grodent, 2015, and Bagenal et al., 2017). Bonfond et al. (2018) inferred that upward electron beams extending to 10 MeV energies were causing what the author termed "bar codes" in the UVS auroral images. It is of interest that these most energetic events seemed to be ordered by the orientation of Jupiter's magnetic dipole tilt with respect to the direction of the sun. Finally, our coverage in space and time is not comprehensive enough to be confident that we have characterized such transient and spatially confined features as the region of auroral flares, hypothesized to map to a magnetic cusp (reviewed by Grodent, 2015, and Bagenal et al., 2017).

3.3 Polar cap electrostatic potentials

The bottom three panels of Figure 3-5 show energetic ion characteristics. Panels (e) and (f) show energy spectrograms, respectively, for combined oxygen and sulfur (O+S), and for protons, both for downward-going ions (within 15° of the downward magnetic field line). Panel (g) shows the pitch angle distributions for O+S. The O+S downward energy spectrogram (e) shows most dramatically the presence of downward going, megavolt potentials discovered by Clark et al. (2017a). There we see downward ion inverted-V's (labeled "MV pot.") with peak values close to or above MeV values in both the northern hemisphere on the left, and in the southern hemisphere on the right. We focus on the O+S rather than the protons because the JEDI energy channels better represent the O+S distributions than they do the H+ distributions for MeV energies. For H+ for the times examined, there is only one energy channel that is above 1 MeV.

The energy distributions within the inverted-V regions are relatively broad, a result of broad energy channels but also of multiple charging of the O and S ion species. According to Clark et al. (2016) O and S charge states are on average about 1.5 and 2.5, respectively, with a distribution of charges for each species. Very crudely we might think of the mean charge state in Figures 3-5 for O+S as being roughly 2, which means that the potential is roughly 0.5 times the mean energy of the inverted-V distribution.

We now realize that these distributions are exceedingly common. Broad regions of megavolt potentials are observed for 80% of the polar cap crossings, north and south (22 out of 28 crossings where the measurements could be made; Figures 3, 4, and 5 show just 6 of those 28 crossings). There are polar cap crossings where we do not see the evidence for the potentials. We do not know whether that condition results from the absence of the potentials or because the ion populations were too sparse to reveal the potentials. The intensities of the downward ions that have revealed the potentials to us are very low.

The potentials seem to hug the center portions of the survey plots, particularly in southern hemisphere. We propose that this is a consequence of spacecraft altitude. Typically the spacecraft is at its lowest altitude near the center of our survey plots. Does the spacecraft need to be below a certain altitude before the megavolt potentials become visible? When we examine the altitude at which the potentials rise or fall (e. g. at ~1020 and 1510 in Figure 3), a fairly consistent pattern prevails in the south with an average transition radial position of 3.6 RJ and a range of 2.4 to 4.6 RJ. A less consistent pattern prevails in the north, with an average transition

radial position of 2.3 RJ and a range of 1.6 to 3.5 RJ. For now our hypothesis that the observation of the megavolt potentials is organized in part by altitude remains plausible but undemonstrated. Note that because of the evolution of the Juno orbit, Juno is spending more time within the southern hemisphere than it is the northern hemisphere, albeit at much higher altitudes, leading to some differences between the north and the south in the trends that we are seeing.

Figure 6 shows the distribution (in red) of the megavolt potentials that we have observed during the first 16 orbits. The projected trajectories where potentials could be measured are shown with thin grey lines. The limited spatial distribution of the megavolt potentials may be real or an artifact of the conditions needed to make the potentials visible. We suspect that both altitude and the availability of sparse populations of heavy ions away from the magnetic equator may play roles in limiting the visibility of the potentials. It appears that neither the position of the sun nor the tilt of the magnetic axis relative to the sun (e. g. Bonfond et al., 2018) play roles.

Clark et al. (2017a) also reported on the occurrence of upward electron inverted-V's within the polar cap, in addition to the downward ion inverted-V's. Electron inverted-V's with monoenergetic peaks as low as 20 – 30 keV have also been identified (Ebert et al. 2017). Such a higher energy electron inverted-V is observed in Figure 4c, labeled "up e- Inverted-V". An expanded view of this region is shown in Figure 7, revealing more details and other instances of inverted-V-type distributions. Several characteristics of these upward inverted-V distributions are worthy of note. First, when the inverted-V distributions appear, the higher electron energies disappear. The electron distributions that are observed, say at the position of the arrow labeled "MeV e- pen." are broadband distributions with energies extending into the MeV energy regime. Again, the feature centered on ~160 keV is the result of those MeV-class electrons penetrating the SSD. At these positions, there is some broadband acceleration process accelerating the electrons up to the spacecraft from below. But when the inverted-V process turns on, the high energy portion of the distributions disappear. This cannot happen if an electrostatic acceleration potential is just added to the acceleration processes. What appears to have happened is that the acceleration mode has changed from a broadband acceleration process to a coherent electrostatic acceleration process. The two processes are not happening at the same time on the same field lines.

A second feature of interest is the position of the upward electron inverted-V's with respect to the positions of the downward ion inverted-V's. The electron inverted-V's with the most classical shapes (e. g. 1830 in Figure 7) tend to occur away from the positions of the downward ion inverted-V's (the original conclusion of Clark et al., 2017a). Here in Figure 7 we see some overlap between the two phenomena at the edge of the region containing the downward ion inverted-V. We also see some more transient electron inverted-V's buried deeply within the region of the downward ion inverted-V. We do not understand the relationship between these two phenomena. The positions of the clearer and "classical" upward electron inverted-V's, like the 1830 event in Figure 7, is shown with blue dots in Figure 6. These are often displaced from the positions of the downward ion inverted-V's.

3.4 Polar cap summary

Examining the polar cap regions observed during Juno's first 16 orbits, we find that:

1) Upward going electron angle beams, with energies often extending into to the MeV range, are consistently present throughout all regions of the polar cap, poleward of the main aurora at Jupiter.
2) There are two separable modes of upward electron acceleration that generate the upward beams in the polar cap: a) broadband acceleration (the most common) generating distributions that are broad and monotonic in energy and encompassing the entire range of JEDI measured energies (~30 – 1200 keV), and b) coherent electrostatic potential upward acceleration generating upward electron inverted-V type distributions. These two mechanisms of upward acceleration are separated spatially; they tend not to occur simultaneously on the same field line.
3) Downward electrostatic electric potentials in the megavolt range are common within the polar cap. Broad spatial regions of such potentials are observed in 80% of the polar cap crossings covering major fractions of the polar cap regions (Figure 6). It is unknown whether the occasional absence of such ion features is due to the absence of the potentials themselves, a function of the altitude of the observations, or the absence of accessible ions needed to illuminate the potentials.
4) The most classic upward electron inverted-V's observed in the polar cap tend to occur in regions separated from, or at the boundaries of, the regions of downward ion inverted-V's that reveal the presence of the megavolt potentials. However, more transient upward electron inverted-V's can occur within the same regions of the megavolt potentials.

4 Main Aurora (MA) Zone

As presented in the Introduction (Section 1) several different energetic particle acceleration characteristics have been previously identified in the literature for the main aurora. However, the commonality, persistence, and ordering of the various features have not been identified. With our more comprehensive examination of the first 10 perijoves, and with the careful consideration of temporal resolution and pitch angle coverage, we now realize that the main aurora has a somewhat repeatable structure. That structuring is shown particularly clearly in Figure 8 (zones identified in Panel d), with a sketch of two newly defined zones presented in Figure 9. Indications of the ordering described here have some presence in the features presented by Allegrini et al. (2017) and Allegrini et al. (2019) using the lower-energy JADE instrument data. We note in particular that the more energetic phenomena discussed here should be viewed as providing tell-tales for the different zones of the aurora. The energetic particles are not necessarily carrying the predominant energy fluxes nor the predominant contributions to the electric currents. Allegrini et al. (2019) focus specifically on the characteristic energies that are carrying the predominant energy fluxes in different parts.

Figure 8 is characteristic of several follow-on figures that we will show, and so we take some time to describe it. It shows, from top to bottom: (a) electron pitch angle distribution averaged over all energies (30-1200 keV) and averaged over 30 seconds, (b) the same electron pitch angle distribution but averaged over 5 seconds, (c) both upward and downward electron energy fluxes for 30-1200 keV electrons averaged over 30 seconds (both sampled within the geometric loss cones), (d) the same upward and downward electron energy fluxes but averaged over 5 seconds, (e) downward electron energy distributions averaged over 1 second (for this particular figure, but not necessarily for others), (f) proton pitch angle

distributions (averaged over energies 50 – 1200 keV), and (g) upward (in this case) proton energy distributions. Note that "upward" and "downward" refer, in all cases, to distributions sampled within the geometric loss cones as estimated using the simple expression presented in Section 2.3. Note in Panel (b) that when we use time averages that are less than 30 seconds, the pitch angle coverage closest to 0° and 180° often have gaps, as shown in white color at the top and bottom edges of the panels. That characteristic leads to some spin modulation in the energy fluxes that are calculated. That spin modulation is often most evident in the upward calculations because the pitch angle structure is often sharpest there. Note also that the color coding in Panels (c) and (d) is according to pitch angle and not according to "upward" and "downward." Black is parallel to the magnetic field and red is antiparallel. Note additionally that in Panels (a) and (b) there is a minimum just at 90° pitch angles. That minimum is a consequence of spacecraft shadowing. The gyro-radii of the electrons with 10's of keV energy are comparable to the large size of the spacecraft, and some near-90° electrons have to travel through spacecraft structures in order to get to the JEDI sensor. Finally, we note that the ion characteristics that we have chosen to show in Panels (f) and (g) will, for other figures, depend on the phenomena that we are trying to highlight. Here we see upward accelerated proton angle beams occurring at the same time of downward electron inverted-V's (IVs in Panel (e)). In this case the proton energy distributions look mostly broadband, but in other cases (in later figures) we do see upward electrostatic acceleration. Note finally that Figure 10 shows global auroral images, which, when combined with some of the auroral images shown in Figures 2-4, provide the context for the main auroral crossings examined in this paper. Figure 10a provides the global auroral context for Figure 8.

4.1 Identification of main aurora zones

The main aurora organizes itself into 3 main zones, identified in Figure 8d with the labels "DifA" for diffuse aurora, ZI(D) for Zone-I (Downward), and ZII(B) for Zone-II (Bi-directional). The schematic in Figure 9 provides a conceptual picture of where the new zones ZI(D) and ZII(B) reside with respect to the jovian system. The diffuse auroral zones reside generally equatorward of the ZI(D) zone. Note that the designations used here (e. g. "zones" rather than "regions", and the use of Roman numerals) are intended to clearly distinguish the corresponding characteristics from numbering schemes used at Earth. In order to identify these zones, one must examine carefully both the pitch angle distributions for the two time resolutions as well as the relative energy fluxes, again for the two different time averages.

The "DifA" zones that tend to occur at the lowest latitudes are the classical "diffuse aurora" zones. The DifA zones are characterized with: (i) electron populations with electron intensities outside of the loss cone larger than the intensities inside the loss cone, and (ii) intensities and energy fluxes within the downward (down-going particles) loss cone greater than the intensities and energy fluxes within the upward loss cone. These zones are interpreted (e. g. Li et al., 2017; Radioti et al., 2009) as occurring because of the existence of magnetically trapped populations of electrons that, as a result of wave-particle interactions, are partially scattered into the loss cone where they impact the atmosphere. The upward loss cone shows lower intensities and energy fluxes because the atmosphere has removed those electrons and prevented them from mirroring back into the upward directions.

Zone-I (ZI(D)), which tends to occur at intermediate latitudes, is characterized with: (i) electron intensities within the downward loss cone greater than the intensities outside of the loss cone, and (ii) downward intensities and energy fluxes greater than the upward intensities

and energy fluxes. The upward loss cone is relatively empty. This zone appears to be the result of an active downward acceleration process (hence the use of the "D" in the shortened designation for this zone) that is not associated with an active upward acceleration process. ZI(D) sometime contains downward electron inverted-V's as seen in Figure 8e with the features labeled "IVs." At other times the acceleration process is broadband. Why we would necessarily categorize the electron inverted-V and downward broadband characteristics into one category (ZI(D)) is discussed below.

Zone-II (RZII(B)), which tends to occur at the higher latitudes, is characterized with: (i) electron intensities within the upward loss cone greater than the intensities outside of the loss cone, (ii) upward intensities and energy fluxes greater than or equal to the downward intensities and energy fluxes, and (iii) downward fluxes sufficient to stimulate observable and sometimes powerful auroral emissions even while the downward energy fluxes are generally no greater than and often less than the upward energy fluxes. This zone appears to be associated with an active upward acceleration process that may also be associated with a somewhat less robust downward acceleration process; the "B" in the shortened designation for this zone refers to "bi-directional." The downward component could correspond to upward acceleration in the opposing hemisphere. Downward proton inverted-Vs sometimes occur in association with ZII(B) (examples shown in later figures). The novelty of observing downward proton inverted-V's contemporaneous with substantial downward fluxes of energetic electrons was highlighted by Mauk et al. (2018).

Poleward of Zone-II (ZII(B)) is what we have identified in earlier discussions as the "polar cap" with upward electron beams (and modest upward energy fluxes still in evidence) but with the downward energy fluxes substantially reduced. However, there is not necessarily a sharp demarcation between ZII(B) and the polar cap. Our positioning of the high latitude ZII(B) boundary is somewhat arbitrary.

For the main auroral crossing shown in Figure 8, Zone-I (ZI(D)) contains the larger downward electron energy fluxes as compared to ZII(B). But there are other crossings where the larger downward energy fluxes occur in Zone-II (ZII(B)). Each zone (ZI(D) and ZII(B)) contains the larger downward electron energy fluxes roughly 50% of the time. One of the reasons that the bi-directional acceleration (Zone-II) has been emphasized in very early Juno publications (special issue of the Geophysical Research Letters introduced by Bolton et al., 2017c) is the fact that the data taken during PJ1 (for unknown reasons) is dominated by Zone-II phenomena, as seen in Figure 11. Here Zone-I is very anemic and lasts for only a very short period of time. For this Zone-II crossing, the downward electron energy fluxes peaked at about 750 mW/m^2 (observable using higher time resolution than shown in Figure 11) even while the upward energy fluxes were even larger (Mauk et al., 2017b). The auroral context for this auroral crossing is shown in Figure 3a (right portion).

4.2 More about Zone-I

While the two phenomena observed with Zone-I, downward electron inverted-V's and downward broadband acceleration, are both characterized with relatively empty upward electron loss cones, it might be questionable to categorize them together into a single zone. One reason that we are comfortable with this grouping is the occasional observation of features showing that these two phenomena really are a part of a single system. As observed during PJ7 (top half of Figure 12), and an event observed during PJ10 (bottom half of Figure 12) we see a very close

association between the electron inverted-V and downward broadband electron acceleration within Zone-I (see Figures 10c and 10d for the auroral contexts for these two events). Specifically, we see the start of a downward electron inverted V (~ 0115:45 for PJ7 and ~1654 for PJ10) that rises up to something like 200 keV to where the electron distribution transitions to a downward broadband distribution. For both cases the upward loss cone is relatively empty for both the inverted-V portions and for the downward broadband acceleration portions. The downward broadband acceleration portion is further identified with (i) the disappearance of the upward proton beam acceleration, and (ii) the fact that the downward electron energy fluxes are greater within the broadband portion than they are during the inverted-V portions. As a side note, notice that in these cases we see what appears to be upward electrostatically acceleration protons occurring in association with the electron inverted-Vs.

Again, it is the very close association between the electron inverted-V's and the downward broadband electron acceleration with these special events that makes us comfortable in grouping these two phenomena into a single extended auroral zone called Zone-I.

4.3 More auroral crossings and auroral electric currents

Additional characteristics of the main auroral structuring are shown in Figure 13 for a PJ6 southern auroral crossing (Figure 10b shows the auroral context). Our identification of the different auroral zones is shown in Figure 13d. Here there is a relatively narrow Zone-I, with a downward energy flux that represents the highest values for the times shown. For Zone-II, unlike the previous examples shown, there is a very clear example of a downward proton inverted-V in Figure 13h, centered near 0658:30. This proton inverted-V peaks at about 200 keV. It is of interest to distinguish between the downward ion inverted-V's observed within the polar cap (Figures 3-5) and those observed within Zone-II (besides the huge differences in particle intensities). The downward ion inverted-V's observed in the polar cap invariably have pitch angle distributions that are very narrowly confined to the field aligned direction (e. g. Figure 3g). The downward ion inverted-V's observed within Zone-II have broad, almost isotropic pitch angle distributions with the exception of a generally empty upward loss cone (Figure 13g). It was hypothesized by Mauk et al. (2018) that the angular distributions were broad because the electrostatic acceleration occurred at very high altitude, resulting in a severe broadening of the angle distributions by mirror forces as the ions propagate downward and then reflect back upward for ions outside of the loss cone. However, no downward ion inverted-V's were observed (Mauk et al., 2018) when we searched for them over the main aurora at higher altitudes (> 4 RJ), even though the features were fairly common at low altitudes. This finding led to the alternative suggestion that the angle distributions of the downward ion inverted-V's had been broadened over the main aurora by wave-particle scattering.

The second significant aspect of Figure 13 is the comparison between the energetic particles-diagnosed auroral zones and the signatures of magnetic field-aligned electric currents presented by Kotsiaros et al., (2019). The top panel of Figure 13 (13a) shows magnetic perturbation data taken directly from that study. These perturbations are interpreted as being caused by magnetic field-aligned electric currents, although a single spacecraft cannot eliminate some contributions from other sources. Kotsiaros et al. (2019) showed both energetic electron data and plasma data in association with these magnetic perturbations, and there were clear correlations between these multiple data sets.

Figure 13 shows that the most intense Zone-I period is very clearly associated with the most intense upward electric currents, as diagnosed with the azimuthal perturbations. Kotsiaros et al. (2019) also noted that this main upward electric current region was observed in association with a pitch angle distribution that we are now associating with Zone-I. Also, the most intense portion of Zone-II (Panel d), and the peak of the downward proton inverted-V (Panel h), are clearly associated with the most intense downward electric currents. Another feature of interest is the slight upturn in the magnetic perturbation just after 0657. There, we see in Panels (d) and (e) a likely (although not assured) brief occurrence of Zone-I buried within the Zone-II. Not all features on the magnetic perturbation profile are matched by the simple zone-ordering described here, but the most intense portion of the energetic particle zones match correspondingly intense magnetic perturbations.

At Earth it is generally thought that coherent upward currents are associated with downward electron inverted-Vs (reviewed by Amm et al., 2002; Paschmann et al., 2002) whereas the electric currents are generally disordered in regions where the electron acceleration is broadband. Here we see a very ordered upward electric current in a region that can support downward electron inverted-V's but here instead is showing downward broadband acceleration. And so, in this respect, Jupiter appears to behave differently from Earth (see also the discussion in Kotsiaros et al., 2019).

Also at Earth, regions of coherent downward electric currents are generally not associated with observable auroral emissions. Here, we see substantial downward electron energy fluxes (Figure 13d) and visible auroral (Figure 10b; the redder structure, more poleward, of the two structures that make up the main aurora near the upper portion) associated with that coherent downward electric current. Again, Earth and Jupiter appear to be behaving very differently.

Because Jupiter's intrinsic, internal magnetic field is so strong relative to the magnetic perturbations associated with auroral currents, the analysis of the auroral-current-generated magnetic perturbations takes substantial effort. The PJ6 data shown in Figure 13a represents the period that has been developed quantitatively to the greatest degree (Kotsiaros et al., 2019). The perturbations for other auroral crossings will be better quantified in the future. For now, the comparison between the stronger magnetic perturbations and the energetic particle auroral zones supports (but does not prove) a hypothesis that Zone-I (ZI(D)) corresponds to upward electric currents, and Zone-II (ZII(B)) corresponds to downward electric currents.

Figure 14 shows one more example of the energetic particle identification of main auroral zones (see Figure 10c for the auroral context). These data were examined in some detail by Mauk et al. (2018) but without the wisdom about auroral zones that we have developed in this paper. Here, Zone-I shows (Panel (e)) a clear example of the downward electron inverted-V in addition to the nearby downward broadband acceleration regions. And also, Zone-II shows a clear example of the downward proton inverted-V (Panel (g)), in association with the strong upward and downward electron acceleration (Panels (a) and (b)). And finally here, the downward electron energy fluxes peak at about the same values for both zones, both being as powerful as any that we have seen within the main auroral regions at Jupiter (> 3 W/m^2; see Mauk et al., 2018 for a discussion of the fact JEDI was close to being saturated during these peaks).

For completeness we include survey plots for two other main auroral crossings in the Supporting Information section with Figures S1 and S2. In examining all of the main auroral

crossings, it is not always possible to be assured of one's identification of the different auroral zones because of incomplete or otherwise poor pitch angle coverage.

4.4 Main Aurora summary

We have found the following phenomenology:

1) Jupiter' main aurora (MA) is organized into three main zones, a Diffuse Auroral zone (DifA) at lower latitudes, a Zone-I (ZI(D)) with mostly downward electron acceleration, generally at intermediate latitudes, and a Zone-II (ZII(B)) at higher latitudes with bi-directional acceleration but with upward fluxes greater than (most often) or equal (less often) to the downward fluxes.
2) The DifA zone is characterized by: (i) electron populations with electron intensities outside of the loss cone larger than the intensities inside the loss cone, and (ii) downward intensities and energy fluxes within the downward loss cone greater than the upward intensities and energy fluxes within the upward loss cone.
3) Zone-I (ZI(D)) is characterized by: (i) electron intensities within the downward loss cone greater than the intensities outside of the loss cone, and (ii) downward intensities and energy fluxes greater than the upward intensities and energy fluxes.
4) Zone-II (ZII(B)) is characterized by: (i) electron intensities within the upward loss cone greater than the intensities outside of the loss cone, (ii) upward intensities and energy fluxes greater than or equal to the downward intensities and energy fluxes, and (iii) even while the downward energy fluxes are generally no greater than and often less than the upward energy fluxes, those downward fluxes are still sufficient to generate observable, and sometimes intense, auroral intensities.
5) For any one main auroral crossing, it is just as likely that Zone-I or Zone-II has the greatest downward electron energy fluxes.
6) Zone-I sometimes shows downward electron inverted-V's with peak energies observed as high as 400 keV (Mauk et al., 2017b) but more often than not the downward acceleration is broadband, with generally greater downward energy fluxes than those supported by the inverted-Vs.
7) Zone-II sometimes shows downward ion inverted-V's with peak energies sometimes up to 400 keV. But often these ion inverted-V's are not evident.

5 Discussion

We return now to our schematic in Figure 9, which again shows our simplified interpretation of the main auroral structures as diagnosed with the energetic particle data and with the associated magnetic perturbation data for PJ6. At the lower latitudes (not shown) are the hot electron populations trapped by Jupiter's magnetic field. Wave-particle scattering causes electron precipitation onto the atmosphere at latitudes below those highlighted in the figure. At intermediate latitudes is a zone (Zone-I or ZI(D)) with downward accelerated energetic electrons that sometimes are broadband in character and other time show the presence of downward electrostatic acceleration in the form of so-called downward electron inverted-V's. For one perijove (PJ6) we demonstrated that this zone is associated with upward magnetic field-aligned electric currents and we hypothesize that this zone is generally associated with such currents. At

still higher latitudes we see a zone (Zone-II of ZII(B)) of bi-directional (up and down) broadband electron acceleration, but more often than not with upward intensities having higher intensities and energy fluxes than the downward values. This zone sometimes shows evidence of downward electrostatic acceleration of ions and sometimes not. For the same perijove (PJ6) we demonstrated that the intense portions of this zone is associated with downward electric currents, and we hypothesize that this zone is generally associated with such currents.

We compare our findings with those of Earth's auroral processes as documented in the broad overview provided by Amm et al. (2002) and Pashmann et al. (2002). At Earth the bright aurora occur in regions of upward currents supporting downward electron inverted-V's and also regions of downward broadband electron acceleration with magnetic turbulence (thought to be Alfvénic) that replaces the clear signatures of magnetic field-aligned currents. At Jupiter we are just as likely to see the brightest aurora associated with Zone-I or Zone-II, associated respectively, (sometimes) with downward and upward electrostatic potentials, and thought to be associated, respectively, with upward and downward electric currents. The symmetry that we see at Jupiter between the ZI(D) aurora and the ZII(B) aurora is unexpected based on Earth observations since strong aurora are not observed at Earth in regions of downward currents or downward electrostatic potentials. Also at Earth, we do not expect to see broadband acceleration associated with coherent and well-ordered magnetic field-aligned currents. For at least PJ6, as shown in Figure 13, we see broadband acceleration in association with the clearest and most coherent signature of upward electron currents (at ~0652).

One of the puzzles of our findings regarding the structuring of the main aurora is why there is such variability in the prominence of each of the two zones (ZI(D) and ZII(B)) with each crossing. Compare, for example, PJ4 in Figure 8 with PJ1 in Figure 11. This variability is a puzzle because Jupiter's aurora is thought to be powered by the steady rotations of Jupiter, and because the upward currents must ultimately be balanced by downward currents. We hypothesize that the apparent imbalances are explained by azimuthal structures within the current system. One of the surprises of the Kotsiaros et al. (2019) findings is that the observed magnetic perturbations (due to magnetic field-aligned Birkeland currents) could only be explained if there were a substantial amount of azimuthal structure within the current system.

The transition between the high latitude boundary of our Zone-II and the Polar Cap, where upward electron angle beams persist, is ambiguous. In drawing the upper ZII(B) boundary in Figures 8, 11, and 13, we have arbitrarily positioned it where the downward intensities become very weak or non-existent. Both ZII(B) and at least portions of the Polar Cap are thought to be regions of upward current, and there may, in fact, be no physical process boundary between these two regions. The distinction may be quantitative rather than qualitative in terms of the availability of plasmas and energetic particle to participate in the processes. It is presumed for example, that the occurrence of downward megavolt potentials close by is a response to the absence of charged particles accessible in the magnetosphere to carry the needed electric currents. The relationship between Zone-II and the polar cap remains an open question.

The results presented here for the main aurora favor greatly observations made on the dusk hemisphere because of the configuration of the Juno orbit thus far. Such phenomena as the

so-called dawn storms are not included. Dawn-side phenomena will be favored later in the mission as the line-of-apsides of the Juno orbit precesses around to the dusk side.

Acknowledgments and Data

We are grateful to NASA and contributing institutions that played critical roles in making the Juno mission possible, and particularly those numerous individuals at The Johns Hopkins University Applied Physics Laboratory (JHU/APL) who developed the JEDI instrument. We are grateful for Lead Engineer Charles E Schlemm and David B. LaVallee for their continued support of JEDI operations. We are grateful to JHU/APL's Lawrence E. Brown and James M. Peachey for their roles in developing and maintaining the data flow and display software used here. This work was funded by NASA's New Frontiers Program for Juno via subcontract with the Southwest Research Institute. The data presented here are available from the Planetary Plasma Interactions Node of NASA's Planetary Data System (https://pds-ppi.igpp.ucla.edu/). Also, ASCII dumps with header documentation has been performed for each panel of the JEDI data displayed in this paper and is accessible at the Juno Science Operations Center at https://pubdata.space.swri.edu/look/0/bace14b1-be59-48e6-92d4-2c6825e05b6f, a URL unique to this paper. The JEDI display software used here is available online and can be accessed by contacting the lead author. A one-hour teleconference tutorial provided by the lead author or his designate is generally sufficient for a user to have sufficient expertise to proceed.

References

Adriani, A. et al. (2017), JIRAM, the Jovian Infrared Auroral Mapper. *Space Sci. Rev.*, 213, Iss. 1-4, pp 393-446, doi:org/10.1007/s11214-014-0094-y.

Allegrini, F. et al. (2017), Electron beams and loss cones in the auroral regions of Jupiter. *Geophys. Res. Lett.*, 44, doi:10.1002/2017GL073180.

Allegrini F. et al. (2019), Electron moments over Jupiter's main auroral emission, Paper SM33G-3299, American Geophysical Union Fall Meeting, December 2019, San Franscico, https://agu.confex.com/agu/fm19/meetingapp.cgi/Paper/600100.

Amm, O. et al. (2002), Chapter 4-In Situ Measurements in the Auroral Plasma. *Space Science Reviews*, 103: 93. doi:10.1023/A:1023082700768 (2002).

Bagenal, F., Adriani, A., Allegrini, F. et al. (2017), Magnetospheric Science Objectives of the Juno Mission. *Space Sci Rev*, 213, Iss. 1-4, pp 219-287, doi:10.1007/s11214-014-0036-8.

Becker, H., Santos-Costa, D., Jorgensen, J.L., et al., Observations of high energy electrons in Jupiter's innermost radiation belts and polar regions by the Juno radiation monitoring investigation: Perijoves 1 and 3. *Geophys. Res. Lett.*, 44, https://doi.org/10.1002/2017GL073091.

Bolton et al. (2017a), The Juno mission. *Space Sci. Rev.*, 213, Iss. 1-4, pp 5-37, doi:org/10.1007/s11214-017-0429-6

Bolton, J. S. et al. (2017b), Jupiter's interior and deep atmosphere: The initial pole-to-pole passes with the Juno spacecraft. *Science*, 356, 6340, 821-825.

Bolton, S., Levin, S., and Bagenal, F. (2017c), Juno's first glimpse of Jupiter's complexity. *Geophys. Res. Lett.*, 44, 7663– 7667, doi:10.1002/2017GL074118.

Bonfond, B. (2012), When moons create aurora: The satellite footprints on giant planets. in Auroral Phenomenology and Magnetospheric Processes: Earth And Other Planets, *Geophys. Monogr. Ser.*, vol. 197, edited by A. Keiling et al., pp. 133–140, AGU, Washington, D. C., doi:10.1029/2011GM001169

Bonfond, B., et al. (2017), Morphology of the UV aurorae Jupiter during Juno's first perijove observations. *Geophys. Res. Lett.*, 44, doi:10.1002/2017GL073114 (2017).

Bonfond, B., Gladstone, G. R., Grodent, D., Gérard, J.-C., Greathouse, T. K., Hue, V., et al. (2018), Bar code events in the Juno-UVS data: Signature ~ 10-MeV electron microbursts at Jupiter. *Geophys. Res. Lett.*, 45, 12,108– 12,115. https://doi.org/10.1029/2018GL080490

Clark, G., B. H. Mauk, C. Paranicas, P. Kollmann, and H. T. Smith (2016), Charge states of energetic oxygen and sulfur ions in Jupiter's magnetosphere. *J. Geophys. Res., Space Physics*, 121, 2264–2273, doi: 10.1002/2015JA022257.

Clark, G., et al. (2017a), Energetic particle signatures of magnetic field-aligned potentials over Jupiter's polar regions. *Geophys. Res. Lett.*, 44, 8703–8711, doi:10.1002/2017GL074366.

Clark, G., et al. (2017b), Observation and interpretation of energetic ion conics in Jupiter's polar magnetosphere. *Geophys. Res. Lett.*, 44, 4419–4425, doi:10.1002/2016GL072325.

Connerney, J. E. P., Acuña, M. H., and Ness, N. F. (1981), Modeling the Jovian current sheet and inner magnetosphere. *J. Geophys. Res.*, 86(A10), 8370– 8384, doi:10.1029/JA086iA10p08370.

Connerney, J. E. P., M. H. Acuña, N. F. Ness, and T. Satoh (1998), New models of Jupiter's magnetic field constrained by the Io flux tube footprint. *J. Geophys. Res.*, 103(A6), 11929–11939, doi:10.1029/97JA03726.

Connerney, JEP, et al. (2017a), Jupiter's magnetosphere and aurorae observed by the Juno spacecraft during its first polar orbits. *Science*, 356, 6340, 826-832, doi:10.1126/science.aam5928.

Connerney, J.E.P., Benn, M., Bjarno, J.B. et al. (2017b), The Juno magnetic field investigation. *Space Sci Rev.*, 213, Iss. 104, pp 39-138, doi:10.1007/s11214-017-0334-z (2017).

Connerney, J. E. P., Kotsiaros, S., Oliversen, R. J., Espley, J. R., Joergensen, J. L., Joergensen, P. S., et al. (2018). A new model of Jupiter's magnetic field from Juno's first nine orbits. *Geophys. Res. Lett.*, 45, 2590– 2596. https://doi.org/10.1002/2018GL077312

Ebert, R. W., Allegrini, F., Bagenal, F., Bolton, S. J., Connerney, J. E. P., Clark, G., … Wilson, R. J. (2017). Spatial distribution and properties of 0.1–100 keV electrons in Jupiter's polar auroral region. *Geophys. Res. Lett.*, 44, 9199– 9207, https://doi.org/10.1002/2017GL075106

Ebert, R. W., Greathouse, T. K., Clark, G., Allegrini, F., Bagenal, F., Bolton, S. J., et al. (2019). Comparing electron energetics and UV brightness in Jupiter's northern polar region during Juno perijove 5. *Geophys. Res. Lett.*, 46, 19– 27. https://doi.org/10.1029/2018GL081129

Elliott, S. S., Gurnett, D. A., Kurth, W. S., Clark, G., Mauk, B. H., Bolton, S. J., … Levin, S. M. (2018a). Pitch angle scattering of upgoing electron beams in Jupiter's polar regions by whistler mode waves. *Geophys. Res. Lett.*, 45, 1246– 1252. https://doi.org/10.1002/2017GL076878

Elliott, S. S., Gurnett, D. A., Kurth, W. S., Mauk, B. H., Ebert, R. W., Clark, G., et al. (2018b). The acceleration of electrons to high energies over the Jovian polar cap via whistler mode wave-particle interactions. *Journal of Geophysical Research: Space Physics*, 123, 7523– 7533. https://doi.org/10.1029/2018JA025797.

Gladstone, G.R., Persyn, S.C., Eterno, J.S. et al. (2017a), The Ultraviolet Spectrograph on NASA's Juno Mission, *Space Sci Rev.*, 213, Iss. 1-4, pp 447-473, doi:10.1007/s11214-014-0040-z

Gérard, J.-C., Bonfond, B., Mauk, B., Gladstone, G. R., Yao, Z. H., Greathouse, T. K., et al (2019). Contemporaneous observations of Jovian energetic auroral electrons and ultraviolet emissions by the Juno spacecraft. *Journal of Geophysical Research: Space Physics*, 124. https://doi.org/10.1029/2019JA026862

Gershman, D. J., Connerney, J. E. P., Kotsiaros, S., DiBraccio, G. A., Martos, Y. M., F.-Viñas, A., et al. (2019). Alfvénic fluctuations associated with Jupiter's auroral emissions. *Geophysical Research Letters*, 46, 7157– 7165. https://doi.org/10.1029/2019GL082951.

Grodent, D. (2015), A brief review of ultraviolet auroral emissions on giant planets. *Space Science Reviews*, 187, 23–50, DOI: 10.1007/s11214-014-0052-8.

Grodent, D., Clarke, J. T., Waite, J. H. Jr., Cowley, S. W. H., Gérard, J.-C., & Kim, J. (2003). Jupiter's polar aurora emissions. *Journal of Geophysical Research*, 108(A10), 1366. https://doi.org/10.1029/2003JA010017.

Haggerty, D. K., Mauk, B. H., Paranicas, C. P., Clark, G., Kollmann, P., Rymer, A. M., Bolton, S. J., Connerney, J. E. P., and Levin, S. M. (2017), Juno/JEDI observations of 0.01 to >10 MeV energetic ions in the Jovian auroral regions: Anticipating a source for polar X-ray emission. *Geophys. Res. Lett.*, 44, 6476– 6482, doi:10.1002/2017GL072866.

Kotsiaros, S. et al. (2019), Birkeland currents in Jupiter's magnetosphere observed by the polar-orbiting Juno spacecraft. *Nature Astronomy*, 3(10), doi:10.1038/s41550-019-0819-7.

Kurth, W. S., et al. (2017a). The Juno Waves investigation. *Space Sci. Rev.*, 213, Iss. 1-4, pp 347-392, doi: 10.1007/s11214-017-0396-y.

Kurth, W. S., Mauk, B. H., Elliott, S. S., Gurnett, D. A., Hospodarsky, G. B., Santolik, O., et al. (2018). Whistler mode waves associated with broadband auroral electron precipitation at Jupiter. *Geophysical Research Letters*, 45, 9372– 9379. https://doi.org/10.1029/2018GL078566

Lanzerotti, L. J. et al. (1993), Measurements of hot plasmas in the magnetosphere of Jupiter. *Planetary and Space Science*, 41 (11-12) pp893-917, doi:10.1016/0032-0633(93)90096-K

Li, W., Thorne, R. M., Ma, Q., Zhang, X.-J., Gladstone, G. R., Hue, V., … Bolton, S. J. (2017). Understanding the origin of Jupiter's diffuse aurora using Juno's first perijove observations. *Geophysical Research Letters*, 44, 10,162– 10,170. https://doi.org/10.1002/2017GL075545

Mauk, B. H., et al. (2017a), Juno observations of energetic charged particles over Jupiter's polar regions: Analysis of monodirectional and bidirectional electron beams. *Geophys. Res. Lett.*, 44, 4410–4418, doi:10.1002/2016GL072286.

Mauk, B. H. et al. (2017b), Discrete and broadband electron acceleration in Jupiter's powerful aurora. *Nature*, 549, 66, doi:10:1038/nature23648.

Mauk, B.H., Haggerty, D.K., Jaskulek, S.E. et al. (2017c), The Jupiter Energetic Particle Detector Instrument (JEDI) Investigation for the Juno Mission. *Space Sci Rev*, 213, Iss. 1-4, pp. 289-346, doi:10.1007/s11214-013-0025-3

Mauk, B. H., Haggerty, D. K., Paranicas, C., Clark, G., Kollmann, P., Rymer, A. M., … Valek, P. (2018). Diverse electron and ion acceleration characteristics observed over Jupiter's main aurora. *Geophysical Research Letters*, 45, 1277– 1285. https://doi.org/10.1002/2017GL076901

McComas, D.J., Alexander, N., Allegrini, F. et al. (2017), The Jovian Auroral Distributions Experiment (JADE) on the Juno Mission to Jupiter. *Space Sci Rev*, 213, Iss. 1-4, pp 547-643, doi:10.1007/s11214-013-9990-9.

Mura et al. (2017), Infrared observations of jovian aurora from Juno's first orbits" Main oval and satellite footprints. *Geophys. Res. Lett.*, 44, 5038, doi:10:1002/2017GL072954.

Paranicas, C., Mauk, B. H., Haggerty, D. K., Clark, G., Kollmann, P., Rymer, A. M., et al. (2018), Intervals of intense energetic electron beams over Jupiter's poles. *Journal of Geophysical Research: Space Physics*, 123, 1989– 1999. https://doi.org/10.1002/2017JA025106.

Paschmann, et al. (2002), Chapter 4-In Situ Measurements in the Auroral Plasma. Auroral Plasma Physics, *Space Sciences Series of ISSI* (International Space Sciences Institute), AIP-Press, ISBN 978-94-007-1086-3.

Radioti, A., A. T. Toma´s, D. Grodent, J.-C. Gérard, J. Gustin, B. Bonfond, N. Krupp, J. Woch, and J. D. Menietti (2009), Equatorward diffuse auroral emissions at Jupiter: Simultaneous HST and Galileo observations. *Geophys. Res. Lett.*, 36, L07101, doi:10.1029/2009GL037857.

Szalay, J. R., et al. (2017), Plasma measurements in the Jovian polar region with Juno/JADE. *Geophys. Res. Lett.*, 44, 7122– 7130, doi:10.1002/2017GL072837.

Tetrick, S. S., Gurnett, D. A., Kurth, W. S., Imai, M., Hospodarsky, G. B., Bolton, S. J., Connerney, J. E. P., Levin, S. M., and Mauk, B. H. (2017), Plasma waves in Jupiter's high-latitude regions: Observations from the Juno spacecraft. *Geophys. Res. Lett.*, 44, 4447– 4454, doi:10.1002/2017GL073073.

Figure 1. Trajectory and JEDI-sensor orientation information for the Juno measurements close to and over the poles of Jupiter. (a) Configuration of the 3 JEDI instruments (JEDI-90 or J90, JEDI-270 or J270, and JEDI-A180 or J180). Each instrument contains 6 telescopes, and the pointing of any one telescope at any one time can be characterized with an "azimuth" angle (defined in the panel) and an "elevation" angle (not shown), both relative to the Jupiter Sun Orbit (JSO) coordinate system with "X" pointing to the sun and "Z" pointing perpendicular to Jupiter's orbital plane. (b) Juno's trajectory close to Jupiter for near perijove encounter (PJ1) for the very first orbit expressed in a magnetic coordinate system defined by the dipole component of the JRM09 magnetic field model (from the Supporting Information with Connerney et al., 2019).

Figure 2. Aspects of the discovery of upward electron beams in Jupiter's polar cap regions all taken during Perijove-1 (PJ1). (a) An UV image of Jupiter's northern aurora taken with the Juno Ultraviolet Spectrograph (UVS; Gladstone et al., 2017a). The colors represent different UV spectral bands with red, green, and blue tending to represent the consequences of high, medium and low energy electron precipitation, and white representing a mix of energies (see Gladstone et al., 2017a). The small white circle is positioned over Jupiter's pole, and the yellow dot shows the average direction of the sun relative to that polar position during the image accumulation period. Overlaying the image is the trajectory of Juno mapped along magnetic field lines to Jupiter's upper atmosphere using the JRM09 internal magnetic field model combined with an explicit model of the external field (Connerney et al., 1981). The image was accumulated during

the portion of the trajectory that is shown thicker than the rest of the trajectory. (b) A sample pitch angle distribution of the up-going electron angle beams averaged over 30-1000 keV. (c) Reconstructed (See the Mauk et al., 2018, Supporting Information Section S1) energy spectra for the up-going electron beams as published by Mauk et al. (2017a). The reconstruction uses analytic functional forms to remove the "minimum ionizing" bump near 160 keV that results from penetration of the detector by the higher energy electrons. (d) Dynamic azimuth distribution of the JEDI-measured electrons averaged over 30-1000 keV energies. Azimuth is defined in Figure 1a.

Figure 3. Perijove-1 (PJ1) survey plots highlighting the broad characteristics of energetic particles over the northern and southern polar caps. (a) Northern (PJ1-N) and southern (PJ1-S) UV auroral images (see the Figure 1 caption for further descriptions). (b) Electron azimuth distributions (see Figure 1 caption). (c) Electron energy spectra sampled within 15° of the up-going magnetic field line (centered on 0° and 180° pitch angles in the north and south respectively). (d) Integrated energy fluxes for the up-going and down-going directions, color coded according to pitch angle (red centered on 0° and black centered on 180°). (e) Energy distributions for the combined Oxygen (O) and Sulfur (S) channels of JEDI for within 15° of the down-going magnetic field line. (f) Energy distributions for protons, also within 15° of the down-going magnetic field line. (g) Pitch angle distributions for the combined O and S energy channels of JEDI.

Figure 4. Perijove-3 (PJ3) survey plots highlighting the broad characteristics of energetic particles over the northern and southern polar caps. See the Figure 3 caption for further information.

Figure 5. Perijove-8 (PJ8) survey plots highlighting the broad characteristics of energetic particles over the northern and southern polar caps. See the Figure 3 caption for further information.

Figure 6. Distribution (shown in red) of downward megavolt potentials observed over Jupiter's northern (a) and southern poles (b) during the first 16 Perijoves of Juno at Jupiter. The thin grey lines show the projected Juno trajectory wherever the JEDI instrument was in a configuration where it could measure the potentials. The large blue dots are centered where the clearer examples of the upward electron inverted-V's were observed. The blue lines are the average main auroral regions as characterized by the Hubble Space Telescope (Bonfond et al., 2012), however those average main auroral positions are often poor indicators of the position of the polar cap. .

Figure 7. The southern portion of the survey plot (for Perijove-3) shown in Figure 4. See Figure 3 caption for further information.

Figure 8. A survey plot for a crossing of the main southern main aurora during Perijove-4 (PJ4). See Figure 10a for the auroral context. (a) Electron pitch angle distribution averaged over 30 second intervals and averaged over energies from ~30 to 1200 keV. (b) The same electron pitch angle distributions averaged over 5 second intervals. (c) Upward and downward integrated energy fluxes (30-1200 keV) averaged over 30 seconds and for sensor mean look directions that reside within 22° of the magnetic field line. The nominal loss cone was about 27°. (d) Same as

(c) but averaged over 5 seconds. (e) Electron energy spectra for downward directions within 22° of the downward magnetic field line, averaged at a 1 second cadence. (f) Proton pitch angle distributions averaged over energies from 50-1200 keV. (g) Energy spectra for up-going protons within 22° of the magnetic field line.

Figure 9. Schematic showing the two zones, (Zone-I or ZI(D) and Zone-II or ZII(B)) and some of their characteristics of the phenomena occurring over Jupiter's main aurora.

Figure 10. Auroral UV images to provide context for several of the main auroral crossings highlighted in this paper. See the Figure 2 caption for a description of the images. The yellow dashed circles highlight the portions of the images that are most relevant to the auroral crossing examples, specifically in (a) Figure 8, (b) Figure 13, (c) Figures 12 and 14, and (d) Figure12.

Figure 11. A survey plot for a crossing of the main southern aurora during Perijove-1 (PJ1-south). Descriptions of the panels can be found in the Figure 8 caption. See Figure 3a (right) for the auroral context.

Figure 12. Perijove-7 north (top) and Perijove-10 north (bottom) examples of when an electron inverted-V distribution (panels (b) and (f)) transitions to a broadband distributions. (a and d) Electron pitch angle distributions. (b and f) Downward electron energy distributions sampled within 22° and 30° of the magnetic field direction. Note that pitch angle sampling for PJ10 required us to include pitch angles outside of the geometric loss cone. (c and g) Estimated downward electron energy fluxes for electrons within 22° and 30° of the magnetic field line. (d and h) Upward proton energy distributions for protons sampled within 30° of the magnetic field line. See Figures 10c and 10d for the auroral contexts.

Figure 13. A survey plot for a crossing of the main southern main aurora during Perijove-6 (PJ6). See the Figure 8 caption for a description of most of the panels. Panel (a) however is new. It shows the azimuthal perturbations of the local magnetic field vector as reproduced from Kotsiaros et al., (2019; their Figure 3). See Figure 10b for the auroral context. Upward and downward are defined for this example as being within 21° of the field line.

Figure 14. A survey plot for a crossing of the main northern main aurora during Perijove-7. See the Figure 8 caption for a description of the panels. See Figure 10c for the auroral context. Upward and downward are defined for this example as being within 22° of the magnetic field line.

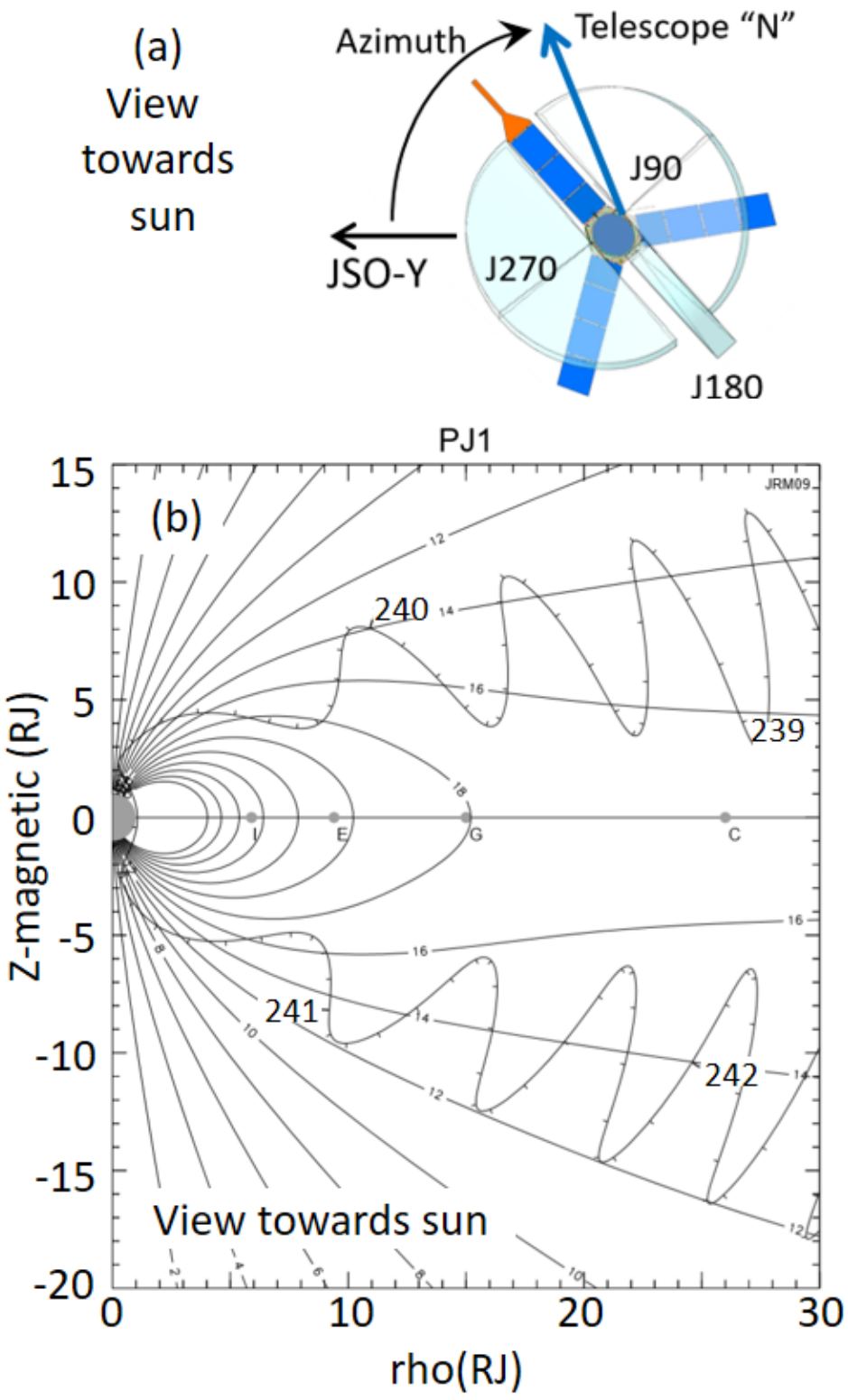
(a)
View
towards
sun
Azimuth
Telescope "N"
J90
J270
JSO-Y
J180
PJ1
(b)
JRM09
240
239
241
242
I
E
G
C
View towards sun
Z-magnetic (RJ)
rho(RJ)
15
10
5
0
-5
-10
-15
-20
0
10
20
30

Figure 1

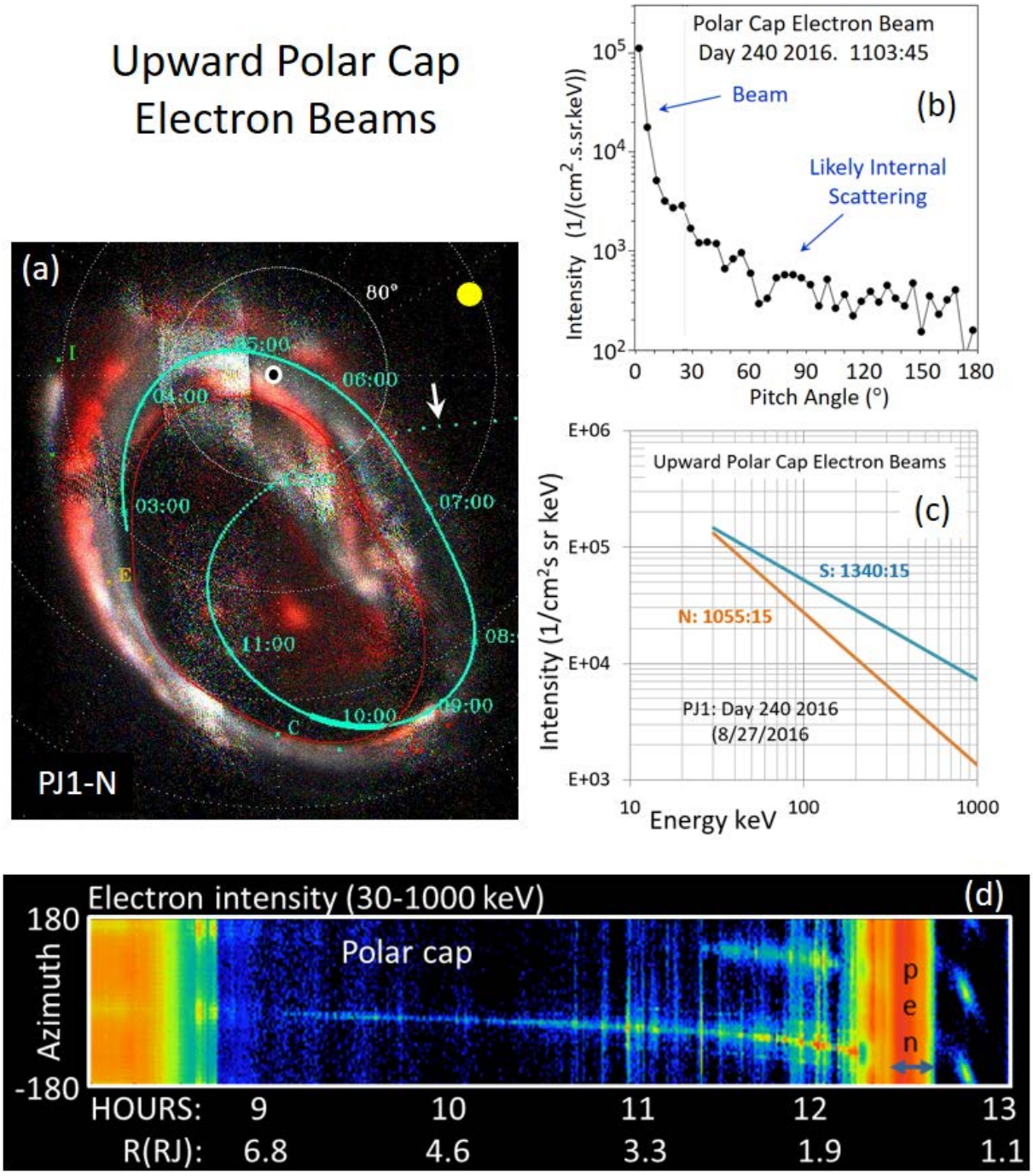
Upward Polar Cap
Electron Beams
(a)
80°
05:00
06:00
04:00
03:00
07:00
11:00
10:00
09:00
PJ1-N
Polar Cap Electron Beam
Day 240 2016. 1103:45
Beam
Likely Internal
Scattering
(b)
Intensity (1/(cm².s.sr.keV))
Pitch Angle (°)
Upward Polar Cap Electron Beams
(c)
S: 1340:15
N: 1055:15
PJ1: Day 240 2016
(8/27/2016
Intensity (1/cm²s sr keV)
Energy keV
Electron intensity (30-1000 keV)
(d)
Polar cap
Azimuth
HOURS:
R(RJ):

Figure 2

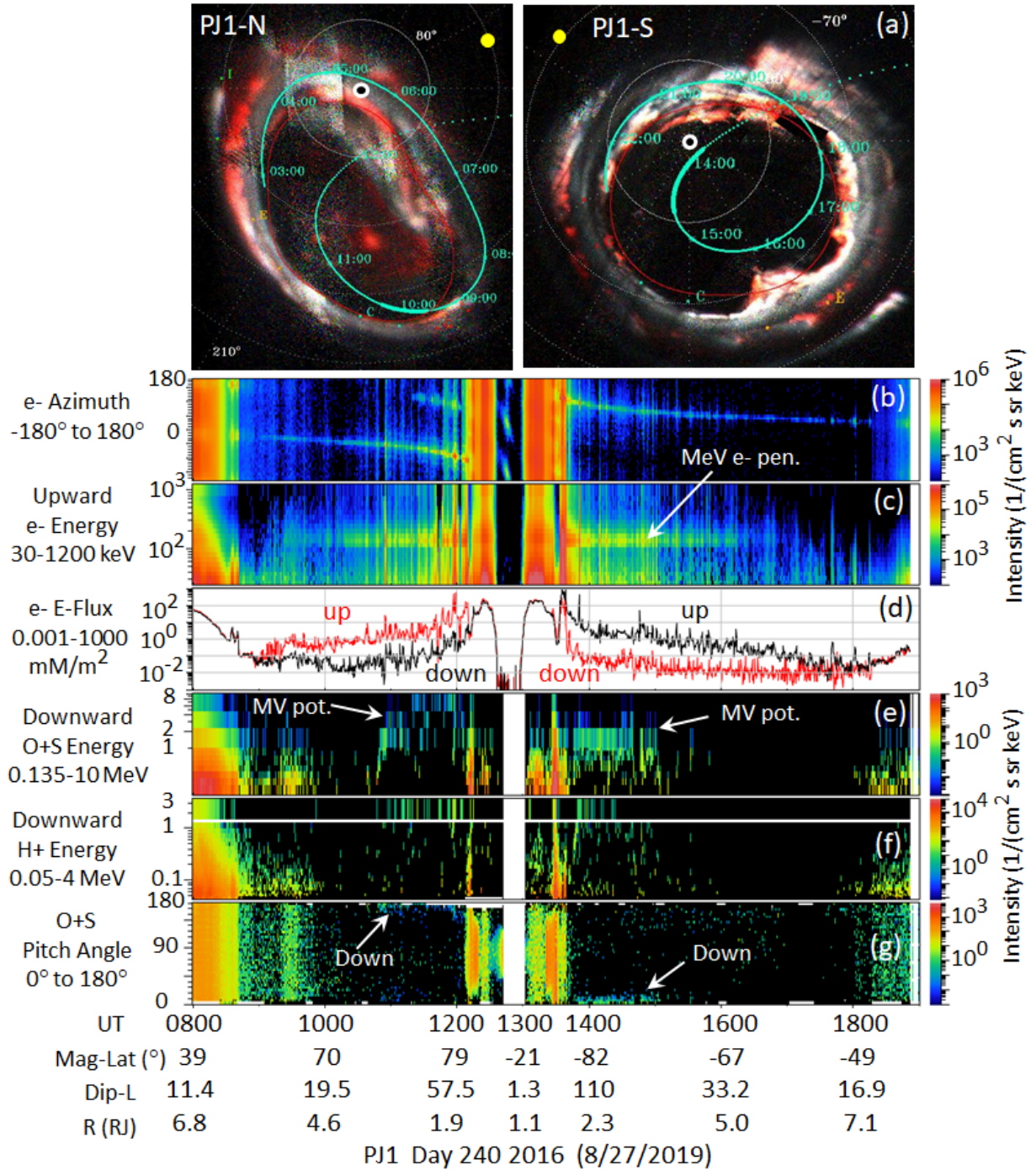
PJ1-N
PJ1-S
(a)
(b)
(c)
(d)
(e)
(f)
(g)
e- Azimuth
-180° to 180°
Upward
e- Energy
30-1200 keV
e- E-Flux
0.001-1000
mM/m2
Downward
O+S Energy
0.135-10 MeV
Downward
H+ Energy
0.05-4 MeV
O+S
Pitch Angle
0° to 180°
MeV e- pen.
up
down
MV pot.
Down
Intensity (1/(cm2 s sr keV)
UT
0800
1000
1200
1300
1400
1600
1800
Mag-Lat (°) 39 70 79 -21 -82 -67 -49
Dip-L 11.4 19.5 57.5 1.3 110 33.2 16.9
R (RJ) 6.8 4.6 1.9 1.1 2.3 5.0 7.1
PJ1 Day 240 2016 (8/27/2019)

Figure 3

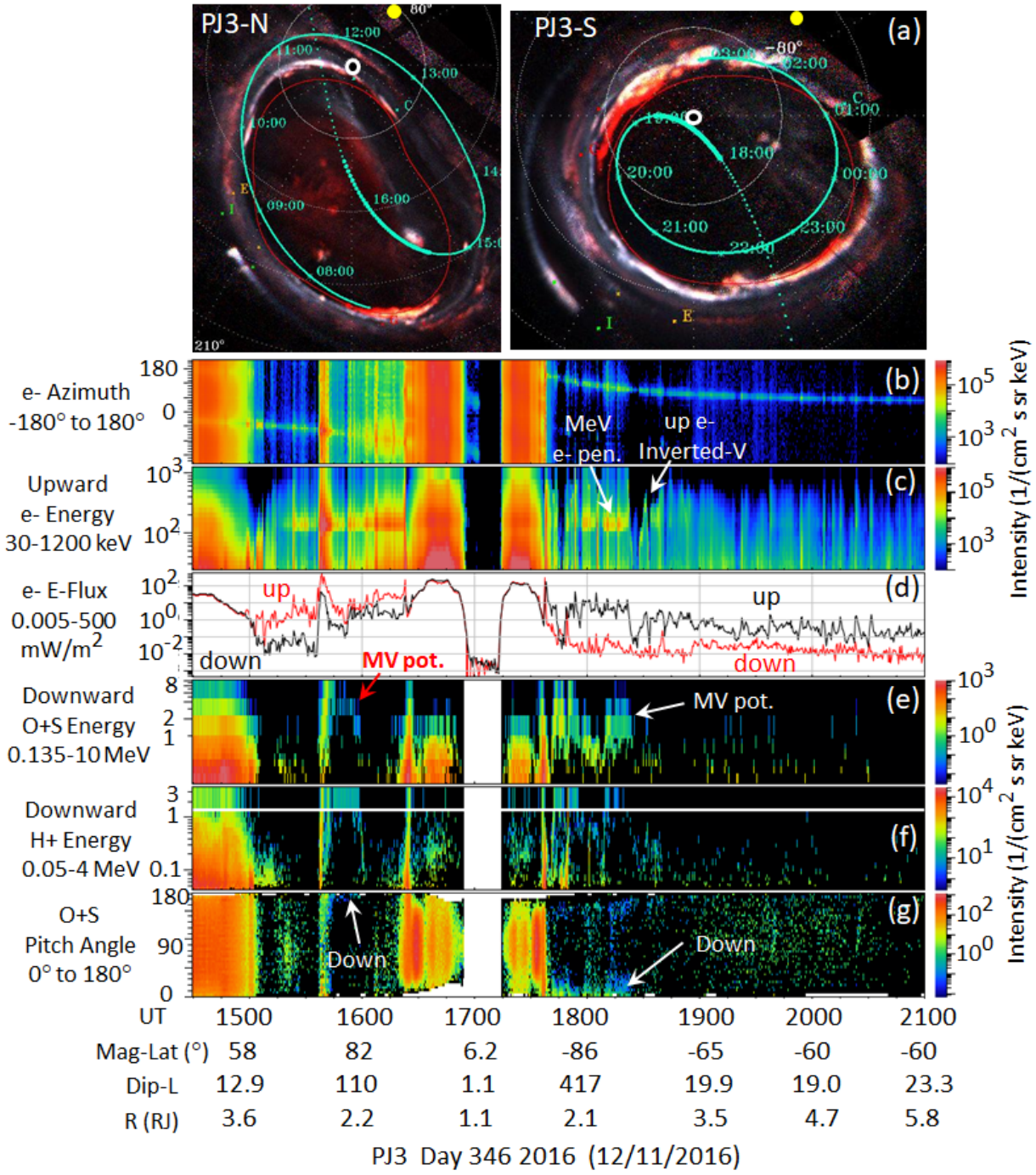
PJ3-N
PJ3-S
(a)
(b)
(c)
(d)
(e)
(f)
(g)
e- Azimuth
-180° to 180°
Upward
e- Energy
30-1200 keV
e- E-Flux
0.005-500
mW/m2
Downward
O+S Energy
0.135-10 MeV
Downward
H+ Energy
0.05-4 MeV
O+S
Pitch Angle
0° to 180°
MeV
e- pen.
up e-
Inverted-V
up
down
MV pot.
Down
Intensity (1/(cm2 s sr keV)
UT
1500
1600
1700
1800
1900
2000
2100
Mag-Lat (°) 58 82 6.2 -86 -65 -60 -60
Dip-L 12.9 110 1.1 417 19.9 19.0 23.3
R (RJ) 3.6 2.2 1.1 2.1 3.5 4.7 5.8
PJ3 Day 346 2016 (12/11/2016)

Figure 4

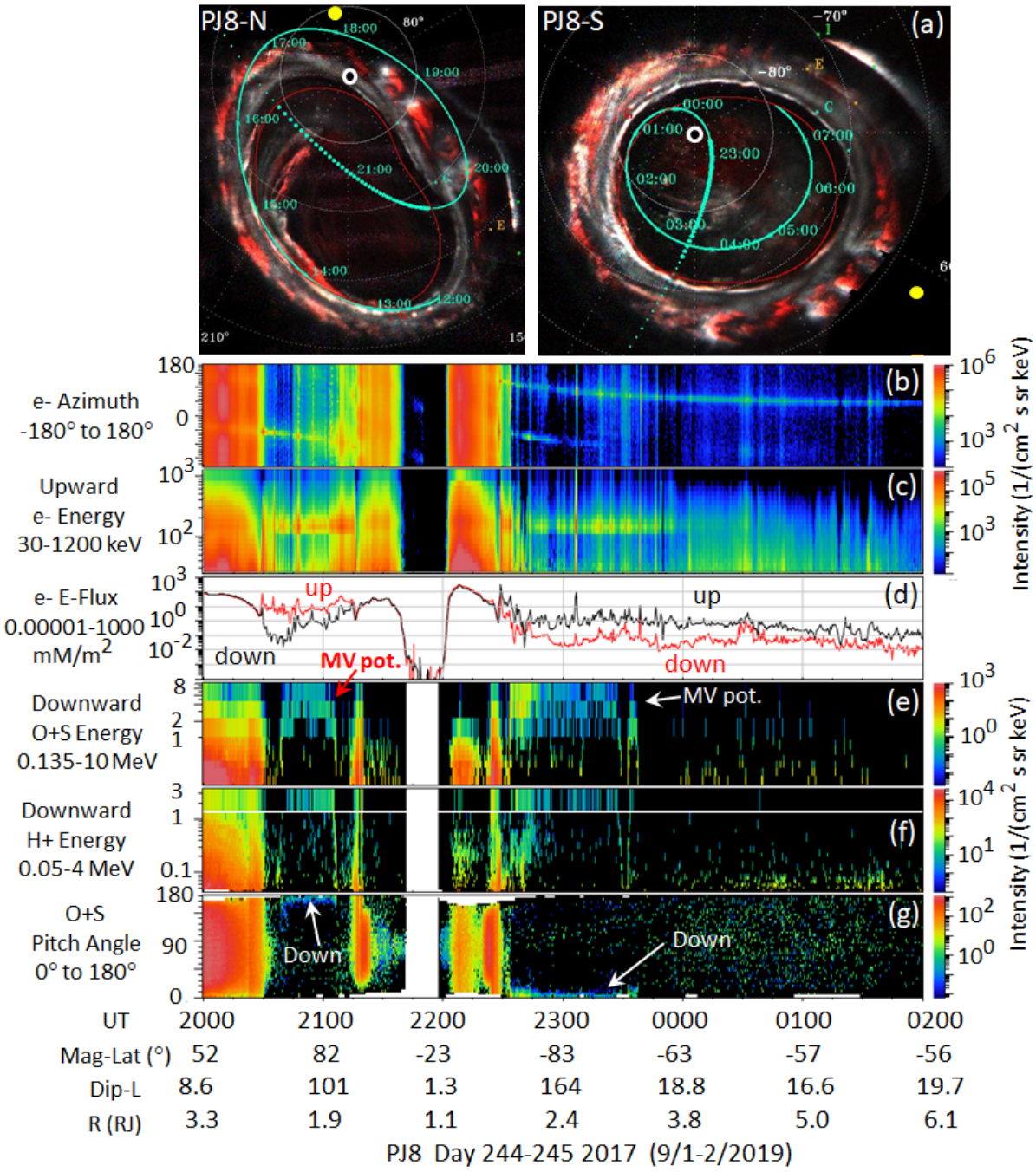
PJ8-N
PJ8-S
(a)
(b)
(c)
(d)
(e)
(f)
(g)
e- Azimuth
-180° to 180°
Upward
e- Energy
30-1200 keV
e- E-Flux
0.00001-1000
mM/m2
Downward
O+S Energy
0.135-10 MeV
Downward
H+ Energy
0.05-4 MeV
O+S
Pitch Angle
0° to 180°
up
down
MV pot.
Down
Intensity (1/(cm2 s sr keV)
UT
Mag-Lat (°)
Dip-L
R (RJ)
2000
2100
2200
2300
0000
0100
0200
52
82
-23
-83
-63
-57
-56
8.6
101
1.3
164
18.8
16.6
19.7
3.3
1.9
1.1
2.4
3.8
5.0
6.1
PJ8 Day 244-245 2017 (9/1-2/2019)

Figure 5

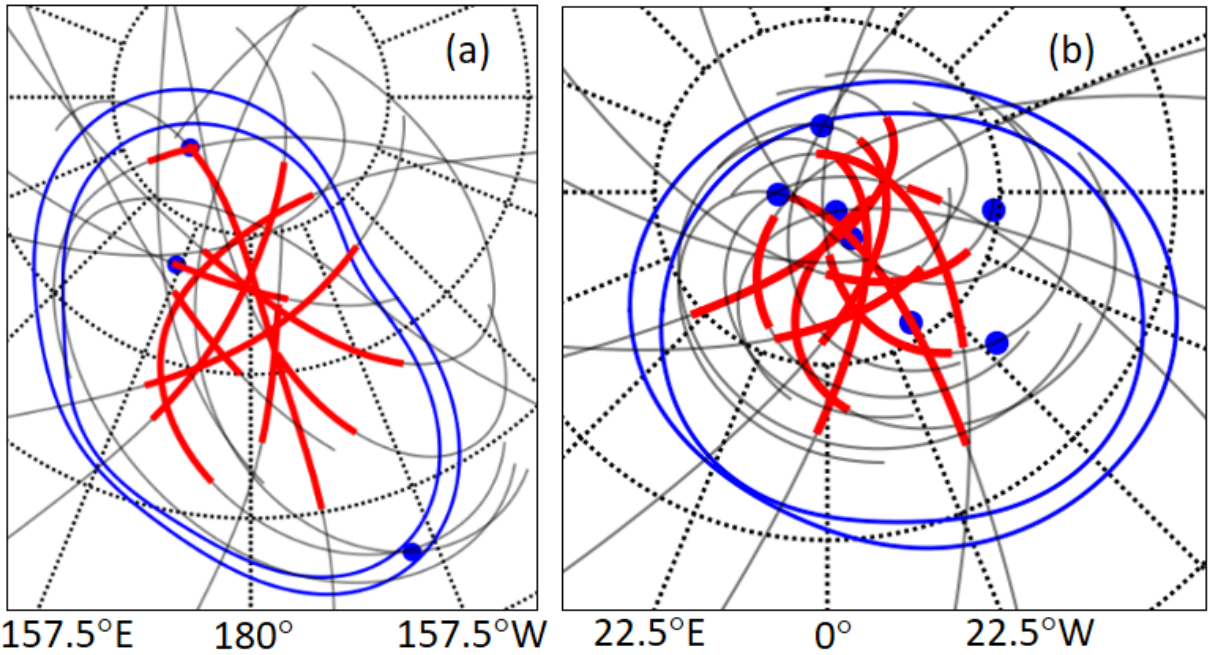

Figure 6

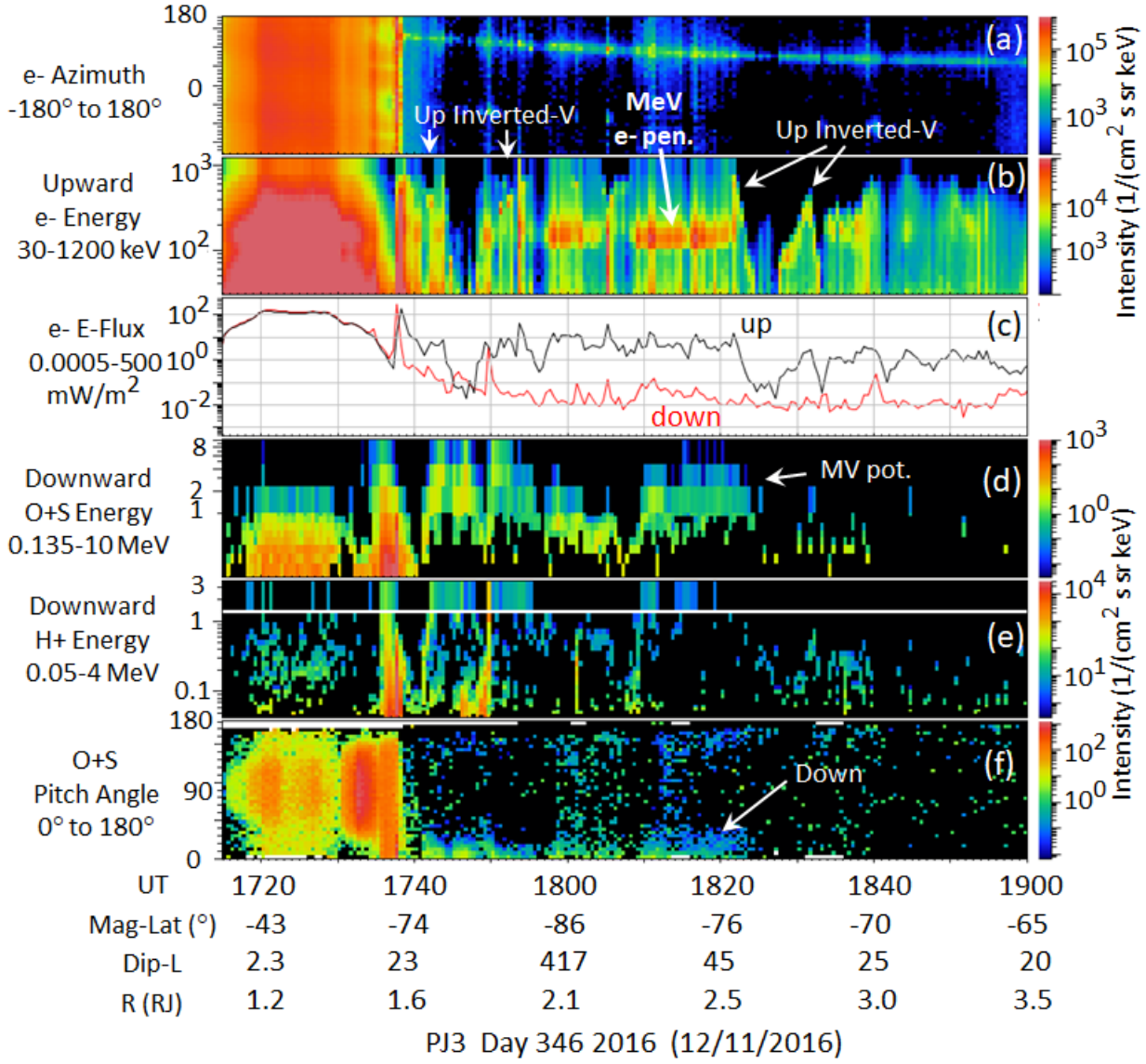
e- Azimuth
-180° to 180°
Upward
e- Energy
30-1200 keV
e- E-Flux
0.0005-500
mW/m2
Downward
O+S Energy
0.135-10 MeV
Downward
H+ Energy
0.05-4 MeV
O+S
Pitch Angle
0° to 180°
Up Inverted-V
MeV
e- pen.
Up Inverted-V
up
down
MV pot.
Down
(a)
(b)
(c)
(d)
(e)
(f)
Intensity (1/(cm2 s sr keV)
Intensity (1/(cm2 s sr keV)
UT 1720 1740 1800 1820 1840 1900
Mag-Lat (°) -43 -74 -86 -76 -70 -65
Dip-L 2.3 23 417 45 25 20
R (RJ) 1.2 1.6 2.1 2.5 3.0 3.5
PJ3 Day 346 2016 (12/11/2016)

Figure 7

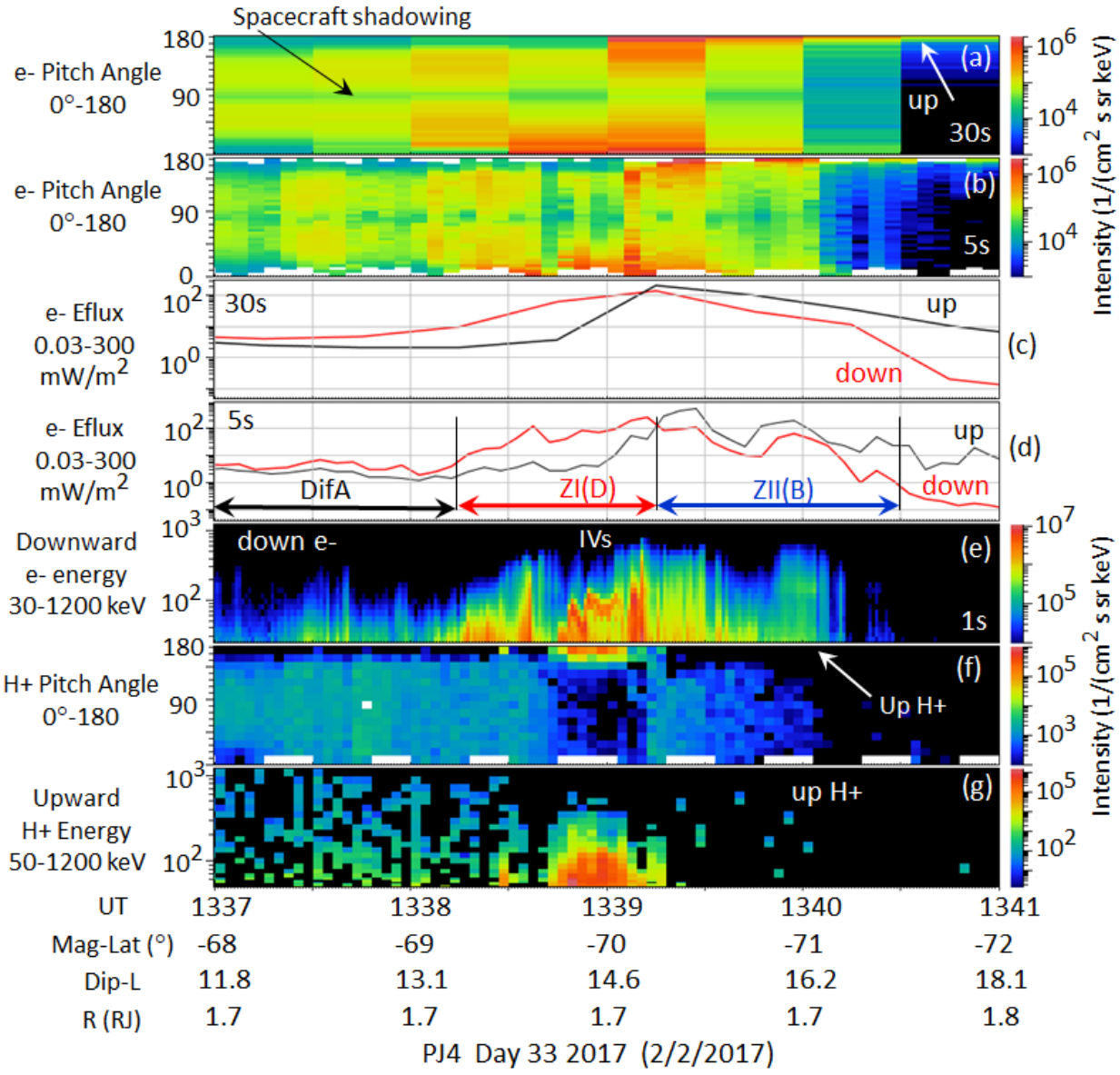
Spacecraft shadowing
e- Pitch Angle 0°-180
180
90
0
(a)
up
30s
(b)
5s
Intensity (1/(cm^2 s sr keV)
e- Eflux 0.03-300 mW/m^2
10^2
10^0
30s
up
down
(c)
5s
DifA
ZI(D)
ZII(B)
(d)
Downward e- energy 30-1200 keV
10^3
down e-
IVs
(e)
1s
10^7
10^5
H+ Pitch Angle 0°-180
(f)
Up H+
Upward H+ Energy 50-1200 keV
up H+
(g)
UT 1337 1338 1339 1340 1341
Mag-Lat (°) -68 -69 -70 -71 -72
Dip-L 11.8 13.1 14.6 16.2 18.1
R (RJ) 1.7 1.7 1.7 1.7 1.8
PJ4 Day 33 2017 (2/2/2017)

Figure 8

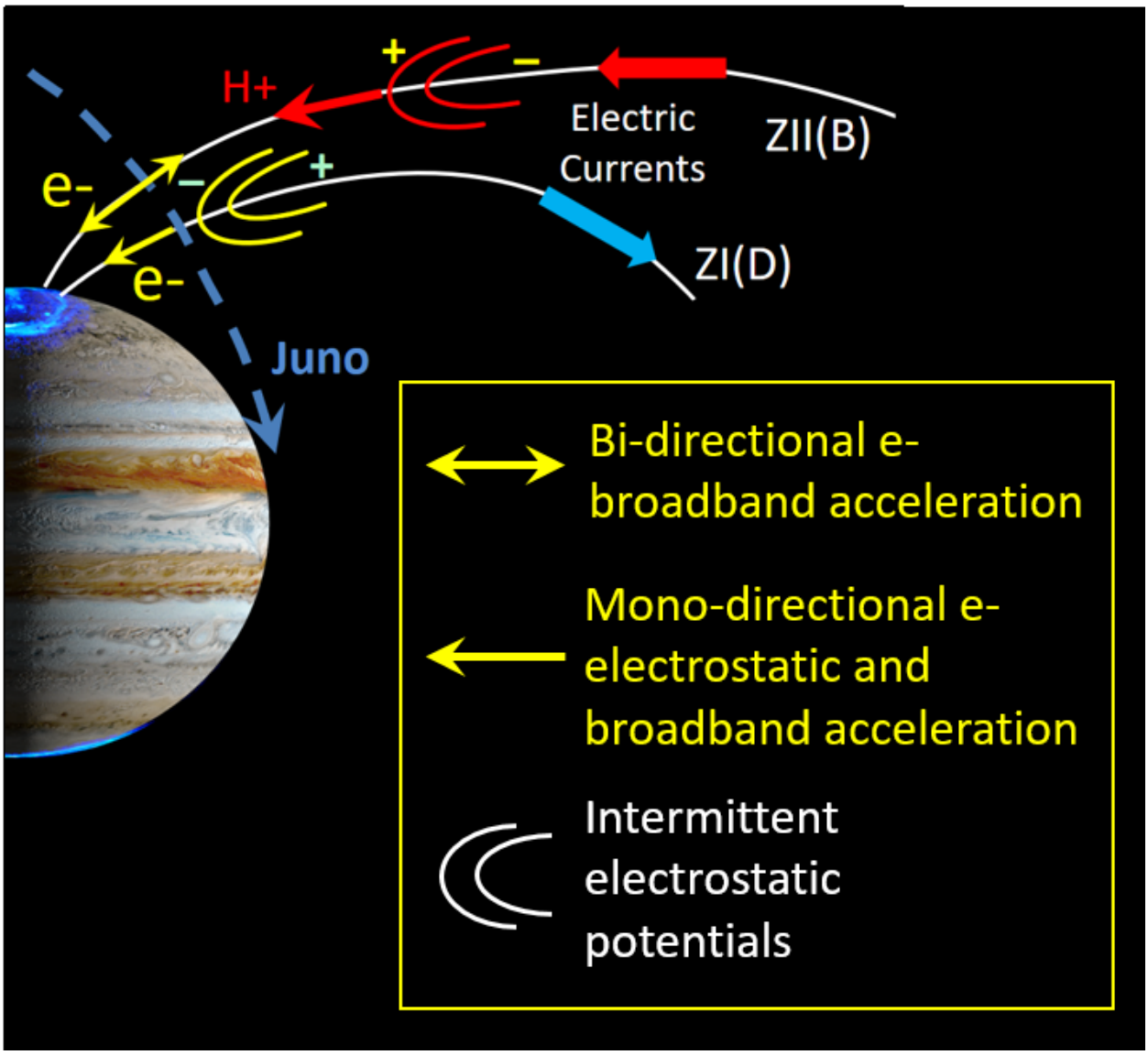
H+
+
−
Electric
Currents
ZII(B)
e-
−
+
e-
ZI(D)
Juno
Bi-directional e-
broadband acceleration
Mono-directional e-
electrostatic and
broadband acceleration
Intermittent
electrostatic
potentials

Figure 9

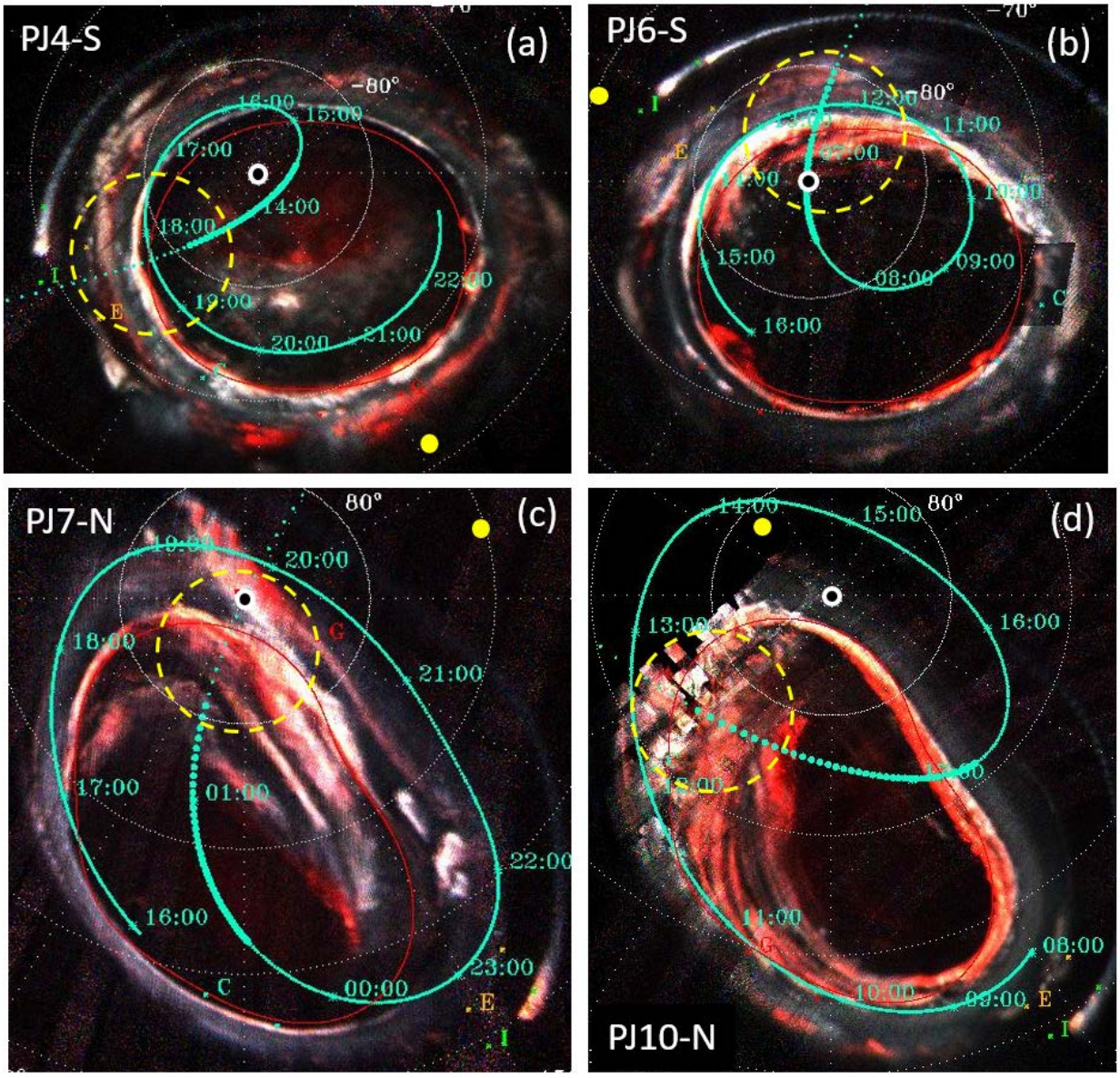
PJ4-S
(a)
−80°
16:00
15:00
17:00
14:00
18:00
22:00
19:00
20:00
21:00
I
E
C
PJ6-S
(b)
80°
12:00
11:00
10:00
15:00
08:00
09:00
16:00
C
PJ7-N
(c)
80°
19:00
20:00
18:00
21:00
17:00
01:00
22:00
16:00
23:00
00:00
C
E
I
(d)
14:00
15:00
80°
13:00
16:00
11:00
08:00
10:00
09:00
E
I
PJ10-N

Figure 10

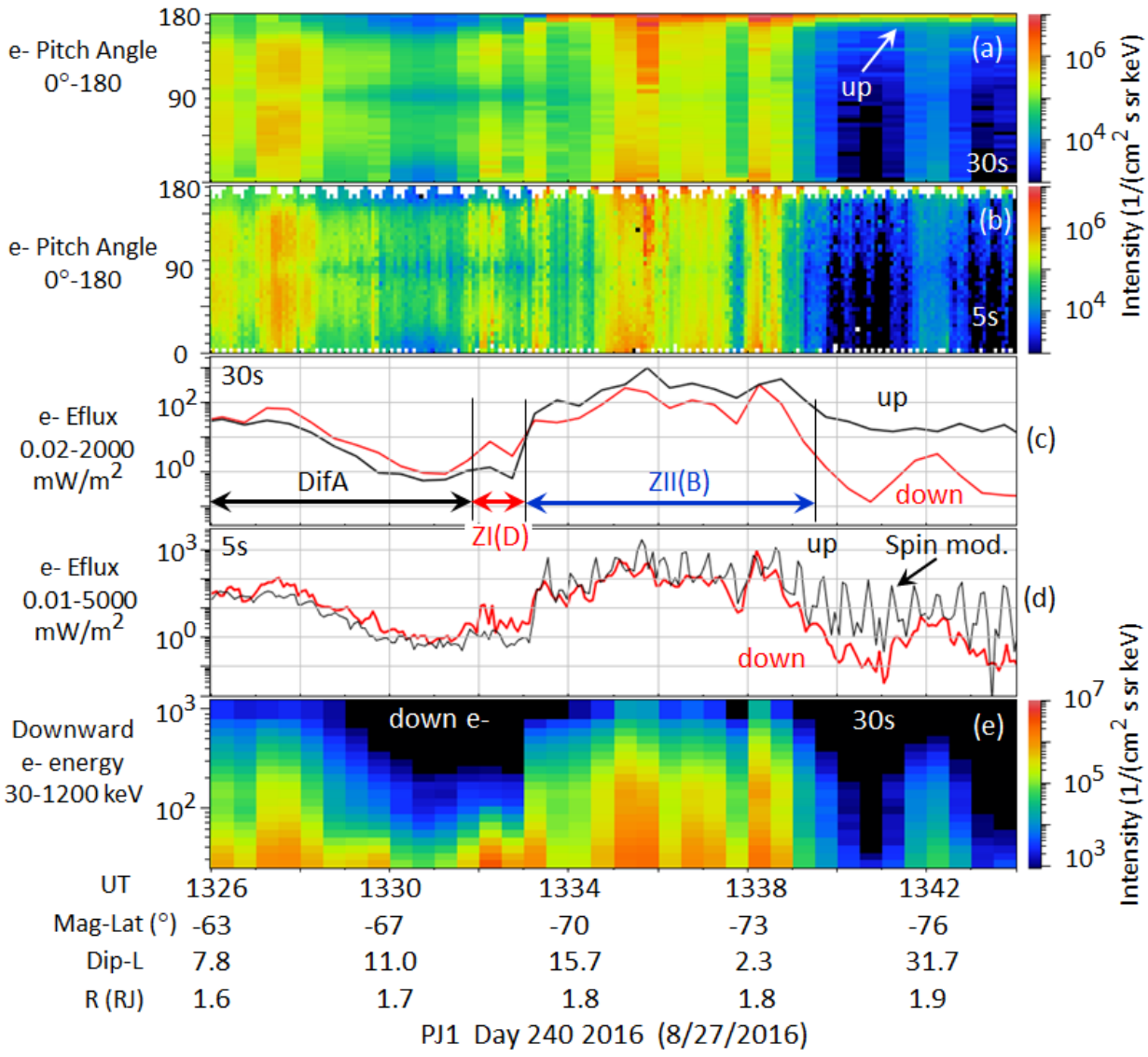
e- Pitch Angle
0°-180
180
90
(a)
up
30s
10^6
10^4
e- Pitch Angle
0°-180
180
90
0
(b)
5s
10^6
10^4
Intensity (1/(cm^2 s sr keV)
e- Eflux
0.02-2000
mW/m^2
30s
10^2
10^0
DifA
ZI(D)
ZII(B)
up
down
(c)
e- Eflux
0.01-5000
mW/m^2
5s
10^3
10^0
up
Spin mod.
down
(d)
Downward
e- energy
30-1200 keV
10^3
10^2
down e-
30s
(e)
10^7
10^5
10^3
Intensity (1/(cm^2 s sr keV)
UT 1326 1330 1334 1338 1342
Mag-Lat (°) -63 -67 -70 -73 -76
Dip-L 7.8 11.0 15.7 2.3 31.7
R (RJ) 1.6 1.7 1.8 1.8 1.9
PJ1 Day 240 2016 (8/27/2016)

Figure 11

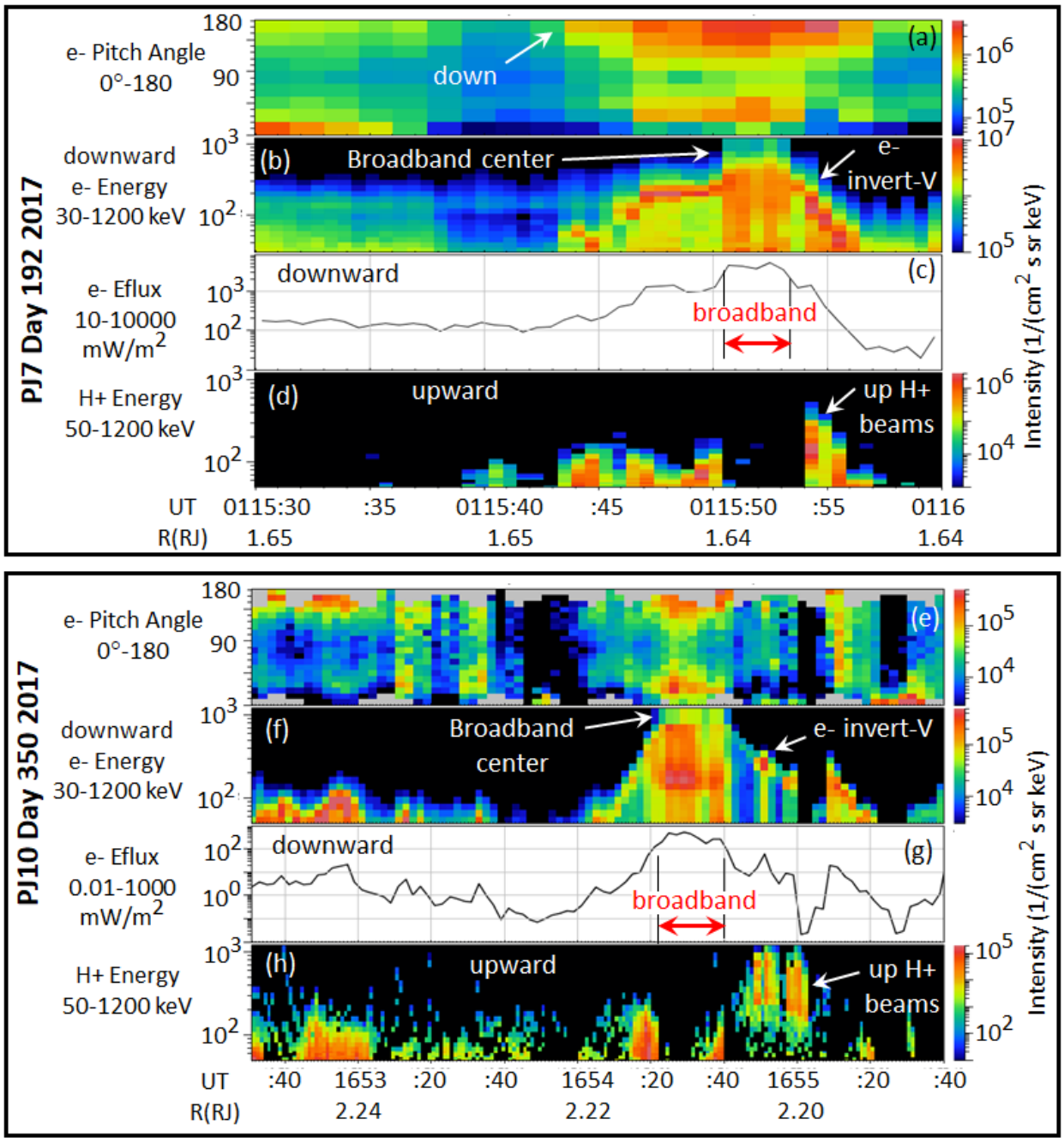
PJ7 Day 192 2017
e- Pitch Angle
0°-180
180
90
down
(a)
downward
e- Energy
30-1200 keV
(b)
Broadband center
e-
invert-V
e- Eflux
10-10000
mW/m2
downward
(c)
broadband
H+ Energy
50-1200 keV
(d)
upward
up H+
beams
Intensity (1/(cm2 s sr keV)
UT 0115:30 :35 0115:40 :45 0115:50 :55 0116
R(RJ) 1.65 1.65 1.64 1.64
PJ10 Day 350 2017
e- Pitch Angle
0°-180
(e)
downward
e- Energy
30-1200 keV
(f)
Broadband
center
e- invert-V
e- Eflux
0.01-1000
mW/m2
downward
(g)
broadband
H+ Energy
50-1200 keV
(h)
upward
up H+
beams
Intensity (1/(cm2 s sr keV)
UT :40 1653 :20 :40 1654 :20 :40 1655 :20 :40
R(RJ) 2.24 2.22 2.20

Figure 12

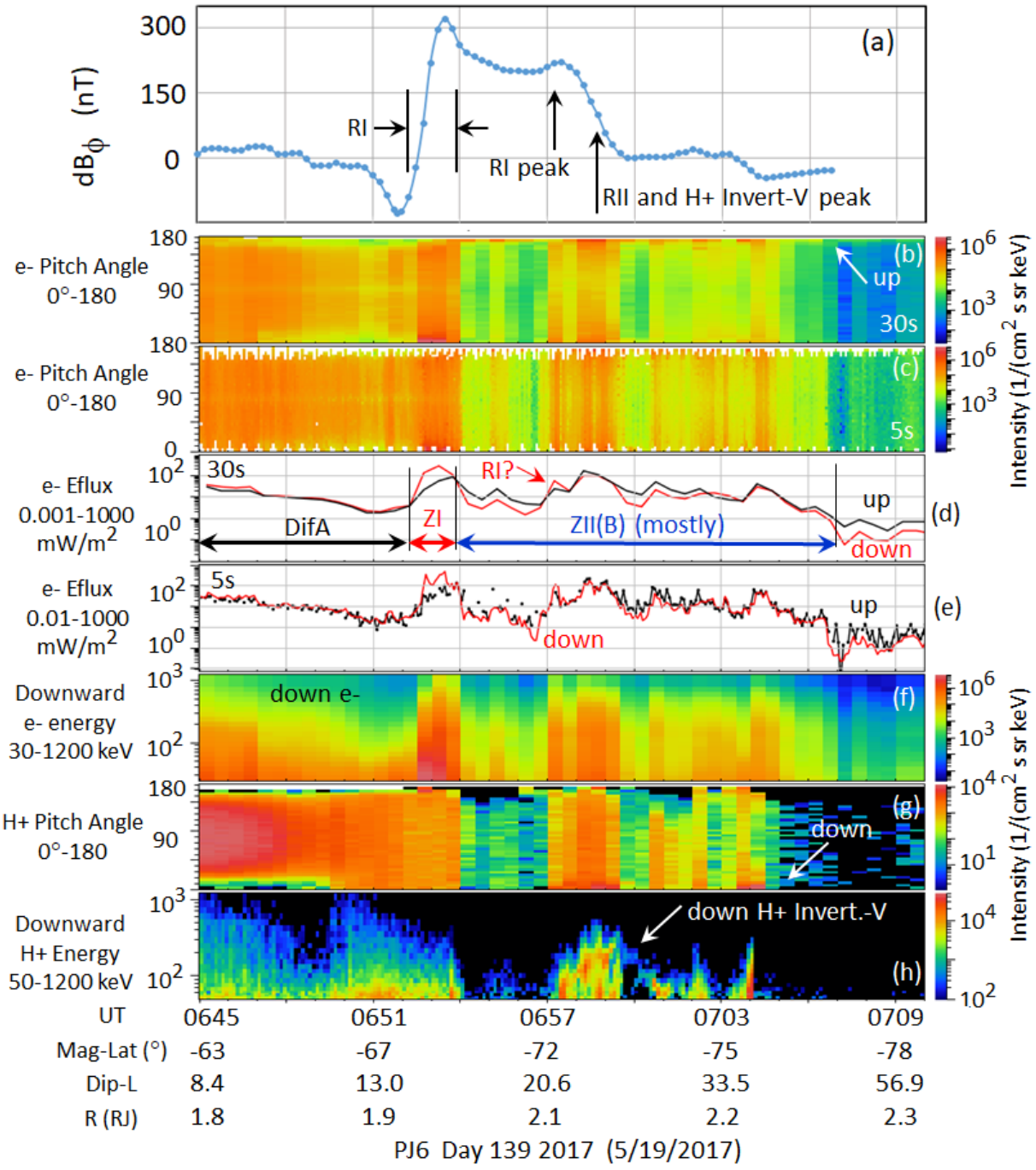
(a)
dBϕ (nT)
300
150
0
RI
RI peak
RII and H+ Invert-V peak
e- Pitch Angle 0°-180
180
90
(b)
up
30s
e- Pitch Angle 0°-180
(c)
5s
Intensity (1/(cm2 s sr keV)
e- Eflux 0.001-1000 mW/m2
30s
RI?
DifA
ZI
ZII(B) (mostly)
up
down
(d)
e- Eflux 0.01-1000 mW/m2
5s
(e)
Downward e- energy 30-1200 keV
down e-
(f)
H+ Pitch Angle 0°-180
(g)
down
Downward H+ Energy 50-1200 keV
down H+ Invert.-V
(h)
UT 0645 0651 0657 0703 0709
Mag-Lat (°) -63 -67 -72 -75 -78
Dip-L 8.4 13.0 20.6 33.5 56.9
R (RJ) 1.8 1.9 2.1 2.2 2.3
PJ6 Day 139 2017 (5/19/2017)

Figure 13

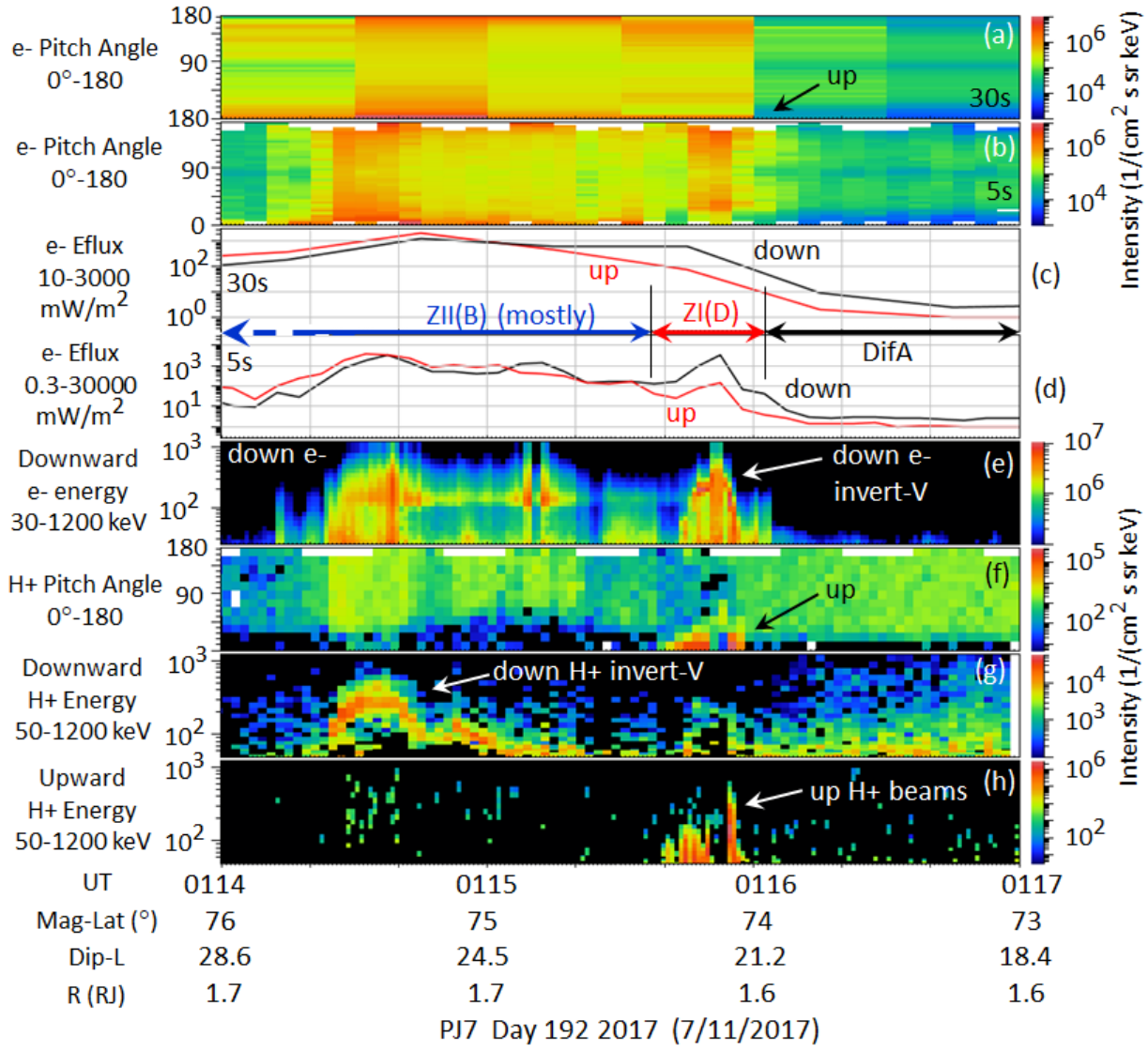
e- Pitch Angle
0°-180
180
90
0
(a)
up
30s
(b)
5s
e- Eflux
10-3000
mW/m2
30s
up
down
ZII(B) (mostly)
ZI(D)
DifA
(c)
e- Eflux
0.3-30000
mW/m2
5s
down
up
(d)
Intensity (1/(cm2 s sr keV)
Downward
e- energy
30-1200 keV
down e-
down e-
invert-V
(e)
H+ Pitch Angle
0°-180
up
(f)
Downward
H+ Energy
50-1200 keV
down H+ invert-V
(g)
Upward
H+ Energy
50-1200 keV
up H+ beams
(h)
UT
0114
0115
0116
0117
Mag-Lat (°)
76
75
74
73
Dip-L
28.6
24.5
21.2
18.4
R (RJ)
1.7
1.7
1.6
1.6
PJ7 Day 192 2017 (7/11/2017)

Figure 14